
Doctoral Dissertations

Student Theses and Dissertations

Spring 2010

Three-body dynamics in single ionization of atomic hydrogen by 75 keV proton impact

Aaron C. LaForge

Follow this and additional works at: https://scholarsmine.mst.edu/doctoral_dissertations

 Part of the [Physics Commons](#)

Department: Physics

Recommended Citation

LaForge, Aaron C., "Three-body dynamics in single ionization of atomic hydrogen by 75 keV proton impact" (2010). *Doctoral Dissertations*. 2313.

https://scholarsmine.mst.edu/doctoral_dissertations/2313

This thesis is brought to you by Scholars' Mine, a service of the Missouri S&T Library and Learning Resources. This work is protected by U. S. Copyright Law. Unauthorized use including reproduction for redistribution requires the permission of the copyright holder. For more information, please contact scholarsmine@mst.edu.

Three-Body Dynamics in Single Ionization of Atomic Hydrogen by
75 keV Proton Impact

by

AARON CHRISTOPHER LAFORGE

A DISSERTATION

Presented to the Faculty of the Graduate School of the
MISSOURI UNIVERSITY OF SCIENCE AND TECHNOLOGY

In Partial Fulfillment of the Requirements for the Degree

DOCTOR OF PHILOSOPHY

in

PHYSICS

2010

Approved by

Michael Schulz, Advisor
Don Madison
Jerry Peacher
Dan Waddill
Jay Switzer

© 2010

Aaron Christopher LaForge

All Rights Reserved

ABSTRACT

Doubly differential cross sections (DDCS) for single ionization of atomic hydrogen by 75 keV proton impact have been measured as a function of the projectile scattering angle and energy loss. This pure three-body collision system represents a fundamental test case for the study of the reaction dynamics in few-body systems. A comparison between theory and experiment reveals that three-body dynamics is important at all scattering angles, and that an accurate description of the role of the projectile-target nucleus interaction as well as the second order projectile-electron interaction remains a major challenge to theory. However, progress is being made in understanding these higher order interactions and a better understanding of the collision dynamics seems possible.

ACKNOWLEDGMENTS

First, I would like to thank my advisor, Dr. Michael Schulz, for giving me a passion for atomic physics and a strong desire to continue to pursue fundamental research in this wonderful field. I am immensely grateful for your continued support. Second, I would like to thank Dr. Ahmad Hasan who basically taught me how to run the experiment from turning on the first power supply to the final data analysis. All of my accomplishments here are directly related to yours and Dr. Schulz' guidance. I would also like to thank the unsung hero (mainly because he doesn't say much) of our group, Kisra Egodapitiya. Your patience and calm demeanor helped to balance my impatience and somewhat animated behavior. Finally, I would like to thank our theoretical collaborators in this work: Drs. Alexander Godunov, Marcelo Ciappina, and Amulya Roy.

I would like to thank my committee members: Drs. Don Madison, Jerry Peacher, Dan Waddill, and Jay Switzer. I would like to especially thank Dr. Jerry Peacher who helped convince me to join the Physics department and offered me the Chancellor's Fellowship. I would also like to thank all of the Physics professors whom I had the pleasure to learn from in the various graduate and undergraduate classes I have taken. I believe the quality of professors in this department is top notch. Finally, I would like to thank my friends: Allison, Andrew, Ben, Ola, Suved, and Tina. You helped make my time in Rolla memorable.

Finally, I would like to thank my family because, without you, I literally wouldn't be here today. I thank you for supporting me in everything I do and know I couldn't make it without you.

TABLE OF CONTENTS

	Page
ABSTRACT	iii
ACKNOWLEDGMENTS	iv
LIST OF ILLUSTRATIONS	vii
SECTION	
1. INTRODUCTION.....	1
2. THEORETICAL MODELS.....	13
2.1. OVERVIEW	13
2.2. CLASSICAL RUTHERFORD SCATTERING	14
2.3. GENERAL CONSIDERATIONS OF QUANTUM MODELS: A PERTURBATIVE APPROACH.....	16
2.4. FIRST AND SECOND BORN APPROXIMATIONS.....	20
2.5. CONTINUUM DISTORTED WAVE-EIKONAL INITIAL STATE MODEL.....	23
2.6. FBA CONVOLUTED WITH CLASSICAL ELASTIC SCATTERING OF THE PT INTERACTION	25
2.7. THREE COULOMB WAVE MODEL.....	26
3. EXPERIMENTAL SETUP.....	28
3.1. OVERVIEW	28
3.2. PROJECTILE BEAM SOURCE AND ACCELERATOR.....	32
3.3. SWITCHING MAGNET AND DECELERATOR.....	35
3.4. PROJECTILE MOMENTUM SPECTROMETER	36
3.5. TARGET BEAM PRODUCTION.....	41

3.6. RECOIL-ION MOMENTUM SPECTROMETER	44
3.7. EXPERIMENTAL EQUIPMENT	48
3.7.1. Position-Sensitive Detectors.....	48
3.7.2. Data Acquisition Electronics	52
4. DATA ANALYSIS	54
4.1. OVERVIEW.....	54
4.2. COINCIDENCE TIME SPECTRUM.....	55
4.3. SCATTERING ANGLE CALIBRATION.....	57
4.4. NORMALIZATION	58
5. RESULTS AND DISCUSSION	60
5.1. OVERVIEW.....	60
5.2. EXPERIMENTAL DD CS_p	60
5.3. THEORETICAL DD CS_p	63
5.4. THEORETICAL ANALYSIS	65
5.5. THEORETICAL DISCUSSION	68
6. CONCLUSIONS AND OUTLOOK.....	78
6.1. CONCLUSIONS.....	78
6.2. OUTLOOK.....	79
BIBLIOGRAPHY	82
VITA.....	88

LIST OF ILLUSTRATIONS

Figure	Page
1.1. Kinematics, precollision and postcollision, of a single ionization event	3
1.2. 3DW-FBA and experimental three-dimensional angular distribution of the emitted electron in 100 MeV/amu $C^{6+} + He$ collisions	6
1.3. Fully differential cross sections for scattering plane and perpendicular plane in 100 MeV/amu $C^{6+} + He$ collisions.....	7
2.1. An ideal two-body collision system showing the dynamics of Coulomb interaction between two charged particles which leads to the incident particles with an impact parameter, b , being deflected by an angle θ	16
3.1. Overhead experimental layout for the PROjectile + Target Ion Momentum Spectrometer(PROTIMS).....	30
3.2. Schematic for kinematically complete experiment on single ionization	30
3.3. Schematic of ion beam source	33
3.4. Force diagram and relative trajectories of various ion species dependent on the ion's charge-to-mass ratio	34
3.5. Schematic of 45° parallel-plate energy analyzer with relative trajectories dependent on the proton energy loss	38
3.6. Vector diagram of \mathbf{p}_o , \mathbf{p}_r , and $\mathbf{q}(=\mathbf{p}_o - \mathbf{p}_r)$	40
3.7. Schematic of the jet region including gas handling system and microwave dissociator.....	41
3.8. Dynamics of gas expansion between two boundaries.	43
3.9. Schematic of recoil ion spectrometer.....	45
3.10. Schematic of a microchannel plate detector and a single channel electron multiplier with electron multiplication dynamics [82]	49
3.11. Schematic of a wedge and strip anode.....	50
3.12. Schematic configuration of MCP and WSA used in experiment	50

3.13. Block diagram of the data collection electronics used for DDCS _p	53
4.1. Coincidence time spectrum with initial time window and random window	55
4.2. The x-component of the projectile position spectrum with a condition on the time peak for H ⁺ before random coincidence subtraction.....	56
4.3. The x-component of the projectile position spectrum with a condition on the time peak for H ⁺ after random coincidence subtraction	57
5.1. DDCS _p as a function of θ_p for fixed energy losses(= 30, 40, 50, 53 eV).....	61
5.2. Average scattering angle as a function of the electron's speed.....	63
5.3. Same as Figure 5.1, but calculations are: dotted curves, CDW-EIS-SC; dashed curves, CDW-EIS-CL; dash-dotted curves, 3C; solid curves, SBA-2C	64
5.4. Same as Figure 5.1, but calculations are: dotted curves, FBA; dashed curves, 2C; dash-dotted curves, SBA; dot-circled curves, EA; solid curves, SBA-2C	71
5.5. Vector diagrams of two classical sequences of interactions leading to PCI involving an interaction between the target nucleus and either the electron or the projectile.....	73
5.6. Same as Figure 5.1, but calculations are: dotted curves, FBA; dashed curves, CDW-EIS-noPT; solid curves, CDW-EIS-SC	74
5.7. Same as Figure 5.1, but calculations are: dotted curves, FBA; dashed curves, 2C; solid curves, 3C.....	75
6.1. Longitudinal recoil-ion momentum distribution with the previous resolution and current resolution	81

1. INTRODUCTION

Atomic collisions have played a critical role in the development of Physics over the past 100 years. Beginning with the famous Rutherford experiment [1], the nature of the atom and its constituents has been studied through collisions involving electrons, ions, and photons. These studies have brought a better understanding of the overall structure of the atom as well as the interactions between its components (electron(s) and the nucleus) and the environment.

However, the significance of collision Physics goes well beyond simply understanding the structure of atoms. In order to understand nature on a fundamental level, one must understand, first, the forces acting in nature and, second, how systems of particles evolve with respect to both time and space under the influence of the underlying interaction. This can easily become a tedious task. In fact, for more than two mutually-interacting particles, it is well established that Schrödinger's equation is unsolvable in closed form even if the underlying force is completely understood. This is known as the few-body problem. Therefore, to solve such systems, including the simplest of systems involving only three particles, requires heavy theoretical modeling and approximations. Rigid experimental data, which measures the properties for all particles in the system, is needed to test the validity of a particular model and its approximations. Atomic collisions are particularly well-suited to studying the few-body problem on the fundamental level for the following two reasons:

First, the force associated with atomic collisions is the electromagnetic force which is essentially completely understood. In contrast, the strong and weak force, both

associated with nuclear systems, are not understood nearly as well as the electromagnetic force. This can lead to an ambiguity as to whether discrepancies between theory and experiment are actually from insufficiently modeling the few-body effects or an incomplete comprehension of the underlying force. For atomic systems, any uncertainties vanish with respect to the force involved. Therefore, the few-body description of theoretical models can be directly tested by experimental data and any disagreements between the two can be related to the few-body problem.

Second, the total number of particles involved in a specific system can be kept small. With a limited number of particles, it is possible to perform a kinematically complete experiment. Conversely, in solid state systems, it is impossible to achieve a complete kinematic description on the atomic scale due to the large number of particles. Because of this dilemma, theorists have to rely on measured quantities statistically averaged over the very large particle number, which could conceal a lack of understanding of the few-body dynamics that would be visible on an individual particle level. Only in atomic few-body systems can one attain a kinematically complete picture of the reaction dynamics without the interpretation being obscured by an incomplete understanding of the underlying forces.

Ionization is an ideal test case of the few-body problem [2,3]. As opposed to other reaction channels such as electron capture and excitation, ionization involves at least three outgoing, unbound particles in the final state. In particular, single ionization provides the simplest few-body process (only three active particles), for which Schrödinger's equation is unsolvable and, consequently, is a benchmark for understanding the most essential components of the few-body problem.

The dynamics for a single ionization event are schematically illustrated in Figure 1.1. A projectile ion collides with the target atom with an initial momentum, \mathbf{p}_0 (Figure 1.1a). The resulting collision leads to ionization of the target atom and a momentum exchange between the three particles due to the Coulomb interaction.

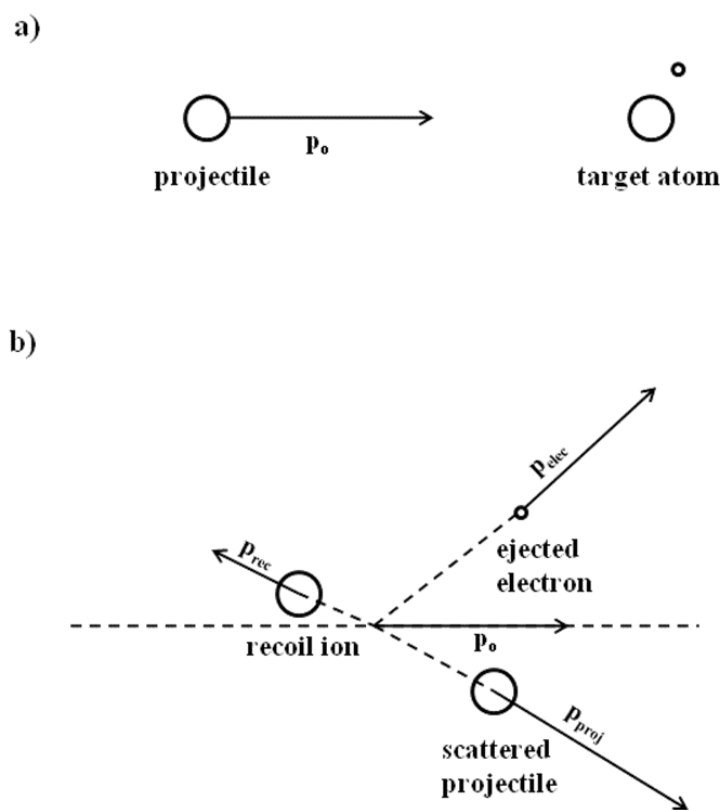


Figure 1.1. Kinematics, precollision (a) and postcollision (b), of a single ionization event.

In order to perform a kinematically complete experiment from a single ionization collision, one must determine the momentum vectors for all three collision fragments in

the outgoing channel (see Figure 1.1b): the scattered projectile, the ejected electron, and the residual target ion. However, only two of the three momentum vectors need to be measured directly while the third momentum vector can be deduced by momentum conservation.

Fully differential cross sections (FDCS) contain all relevant kinematic information about the collision process and are the most sensitive test to theory. The first fully differential measurements for electron impact ionization were taken over 40 years ago through the work of H. Ehrhardt [4] and, for certain conditions, have been in good agreement with theory [5]. For ion impact ionization, it is incredibly difficult to measure the projectile momentum since both the scattering angle and relative energy loss are extremely small. Therefore, fully differential cross sections have only been made available over the past 10 years [2,6-11]. These fully differential measurements were made possible thanks to a new and innovative technique in collision measurement collection known as COLd Target Recoil Ion Momentum Spectroscopy (COLTRIMS) [12,13], which measures the recoil ion momentum in coincidence with either the ejected electron momentum or the projectile momentum.

In the case of electron-impact ionization, major progress in describing the reaction dynamics has been achieved in the last decade. Sophisticated non-perturbative models were developed which treat the entire collision system, including the projectile, fully quantum-mechanically [3,14,15]. However, for ion impact, treating the projectile accurately is much more challenging because a very large number of angular momentum states contribute to the scattered wave as a result of the large projectile mass. More recently, non-perturbative methods were reported for ion impact as well; however they do

not account for the interaction between the projectile and the target nucleus (PT interaction) [16,17]. Since, in actual three-body collision processes, there are interactions between all three particles, a complete theoretical model should include the PT interaction. Only perturbative approaches, accounting for the PT interaction in an approximate manner, are currently available for ion-impact ionization [e.g. 18-19].

Nevertheless, perturbative models were believed to provide an adequate description of the collision dynamics for collision systems where the perturbation parameter η (projectile charge to velocity ratio) is relatively small ($\eta < 1$). However, the surprising observation of qualitative discrepancies between experiment and theory for η as small as 0.1 [2] showed that, for ion impact, theory is still facing significant problems. In Figure 1.2, a fully differential three-dimensional angular distribution of the emitted electron is calculated by theory (a) and measured by experiment (b). The theoretical calculation is the Three Distorted Wave model (3DW), a state-of-the-art perturbative calculation, which treats the entire system quantum mechanically. The distribution shares similar features, namely, a two-lobe structure, seen in fully differential data for other high energy atomic collisions [7,9,10]. The larger lobe, known as the binary peak, results from the electron being emitted in the direction of the momentum transfer \mathbf{q} . This is due to a binary interaction between the ejected electron and the projectile where the electron essentially “absorbs” all of the transferred momentum. Likewise, the smaller lobe, known as the recoil peak, results from the electron being emitted in the direction opposite of \mathbf{q} due to a double scattering process [20]. In this case, the electron is initially emitted in the direction of \mathbf{q} , next, the electron elastically backscatters from the residual target

ion, which thus picks up part of the momentum transferred by the projectile to the target atom.

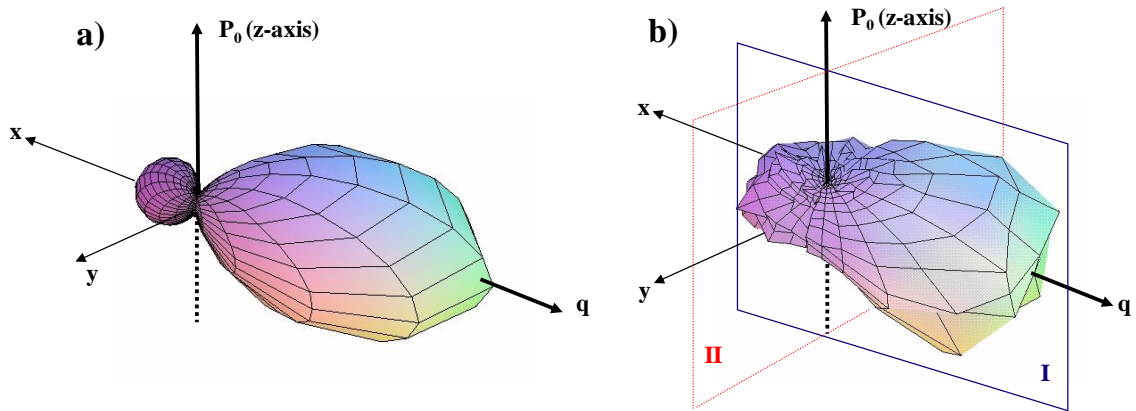


Figure 1.2. 3DW-FBA(a) and experimental (b) three-dimensional angular distribution of the emitted electron in 100 MeV/amu $C^{6+} + He$ collisions. The electron energy is $E_e = 6.5$ eV and the momentum transfer is $q = |P_o - P_f| = 0.75$ a.u. [2]. The planes labeled I and II indicate the scattering plane and the perpendicular plane, respectively.

Figure 1.3 shows two planes in the FDCS of Figure 1.2; the first (a) is the scattering plane, defined by the initial projectile momentum \mathbf{P}_o and the momentum transfer \mathbf{q} , and the second (b) is the perpendicular plane, defined by \mathbf{P}_o and perpendicular to \mathbf{q} . When compared to experimental data for the same system parameters, Schulz et al. [2] found that there was good agreement between theory (dash-dotted line in Figure 1.3a) and experiment in the scattering plane with only slight discrepancies in the recoil peak. However, there was virtually no agreement in the perpendicular plane. The experimental data shows a clear peak structure occurring at 90° , whereas the 3DW model yields an almost isotropic distribution with respect to the emission angle and the calculated magnitude of the cross sections is five times smaller than in experiment. The authors

suggested that these discrepancies were due to higher-order contributions to the collision process, namely the NN interaction. One can explain the experimental angular distribution if the collision is considered to be a two-step process where: 1) an initial binary interaction takes place between the projectile and an electron which leads to its emission, and 2) the projectile is then elastically scattered from the target ion. The additional momentum transferred in the second process is independent of the electron emission direction and can lead to a rotation of the total momentum transfer \mathbf{q} since the elastic scattering can occur at any angle between 0° and 180° . This creates a ring-like feature in the three-dimensional FDCS about the projectile beam axis.

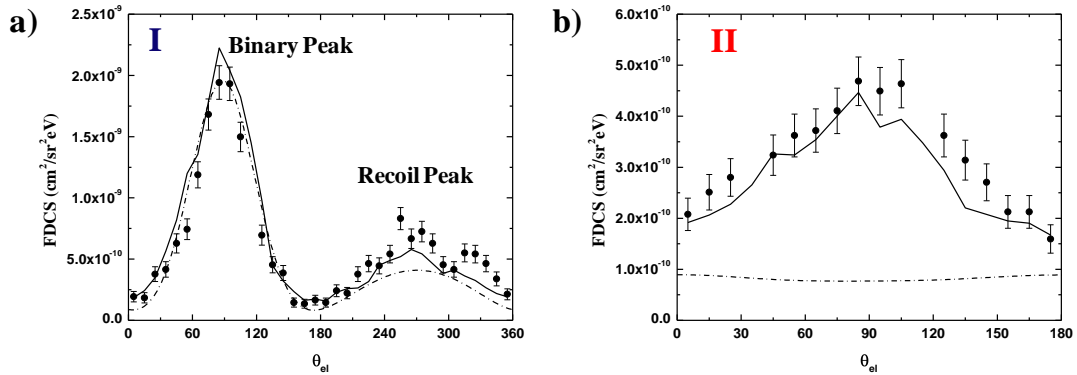


Figure 1.3. Fully differential cross sections for scattering plane (a) and perpendicular plane (b) in 100 MeV/amu $\text{C}^{6+} + \text{He}$ collisions. The electron energy is $E_e = 6.5$ eV and the momentum transfer is $q = |\mathbf{P}_o - \mathbf{P}_f| = 0.75$ a.u. Circles: experimental data; Dash-dotted line: 3DW-FBA; Solid line: FBA convoluted with classic elastic scattering and experimental resolution[37].

The results of 100 MeV/amu $\text{C}^{6+} + \text{He}$ data [2] stimulated further experimental research which was directed at attaining a better understanding of the NN interaction with

varying perturbations in both projectile charge and velocity [7-11, 21-25]. The structure observed in the perpendicular plane was reproduced for other collisions systems [10,23]. At a larger perturbation parameter ($\eta = 0.58, 0.8$), the structure observed in the perpendicular plane actually became larger in size than the recoil peak itself. Furthermore, at very large η , the effects of the NN interaction were even observed in the scattering plane [7,8,21]. Overall, perturbative approaches to resolving the discrepancies between experiment and theory have fallen short of their overall goal [26,27] especially at the above mentioned large η . There is, however, one exception to the overall trend [28]. Voitkiv et al. were able to achieve good overall agreement with experimental data for the 1 GeV/amu $U^{92+}+He$ experiment [10], which is a particularly special system since the projectile approaches relativistic speeds (90% the speed of light). Also, the calculation was only performed for electrons ejected into the scattering plane and, most likely, would not be able to reproduce the structures observed in the perpendicular plane.

More recently, out-of-plane structures were even observed for electron impact ionization for targets of He [29-31] and Mg [32]. For the Mg case, theory [27,32] has had success reproducing the out-of-plane structure seen in experiment using the Distorted Wave Born Approximation (DWBA). However, for the He case, theory has not yet been able to produce a complete picture for the three dimensional angular distribution of the ejected electron [31].

In a recent series of papers [33-35], it was suggested that the large discrepancies seen in both the scattering plane and perpendicular plane were simply due to the experimental resolution. Specifically, in the 3.6 MeV/amu $Au^{53+} + He$ experiment, Olson et al. [33] claimed to be able to reproduce the effects seen in experimental data by

accounting for the target gas temperature. However they assumed a temperature of 16 K, which is approximately one order of magnitude higher than experimentally reported. In the 100 MeV/amu $C^{6+}+He$ data, Fiol et al. [35] stated that the NN interaction played an unimportant role in the overall reaction dynamics and the structure in the perpendicular plane was solely due to experimental resolution. By simply accounting for a 1K target gas temperature, they claimed to be able to resolve any theoretical discrepancies. In response, a comprehensive examination of all aspects of the experimental uncertainties was conducted by M. Dürr et al. [36]. They used a Monte Carlo event generator technique to convolute the experimental uncertainties into the FBA model. This analysis clearly showed that a target temperature of 1K has no significant effect on the measured FDCS. However, the finite overlap between the projectile and target beam does have an effect on the overall resolution. Nevertheless, Dürr et al. clearly demonstrated that the resolution does not fully explain the interesting effects observed in the aforementioned FDCS and found that the peak structure in the perpendicular plane was mostly due to a real physics effect. To make further use of the Monte Carlo event generator technique, Schulz et al. [37] used it to convolute classical elastic scattering between the projectile and target nucleus with the FBA model (solid line in Figure 1.3), in addition to the experimental resolution. Surprisingly, in the 100 MeV/amu $C^{6+}+He$ results, this produced an almost perfect agreement between theory and experiment, which, contrary to the claims of Fiol et al. [35], strongly suggests the importance of the NN interaction in three-body kinematics.

Although the excellent agreement between theory and experiment using classical elastic scattering provides some qualitative insight into the mechanisms of three-body

scattering, it is not a complete theory for understanding the three-body problem. Since the bodies involved (projectile, ejected electron, and residual ion) are quantum mechanical bodies, the theoretical model describing their interaction should, therefore, also be fully quantum mechanical. Until a theory is found that accurately and consistently describes the complete three-particle interaction, the three-body problem remains unsolved.

The reasons for the problems that quantum mechanical theories have for accurately describing even the simplest quantum mechanical system are currently unknown. One possibility is that the complex initial state of Helium is very difficult to incorporate accurately in a collision calculation. The Helium atom has a passive electron in the single ionization process and can, therefore, only be considered to be a “pseudo” three-body system. Another possibility is that the theoretical difficulties actually lie within the quantum mechanical treatment of the three-body problem, in particular, the treatment of the nuclear-nuclear interaction. In order to test the two hypotheses, it is necessary to perform an experiment on a “pure” three-body system.

Due to the previously stated difficulties pertaining to the fundamentally important few-body problem, accurate and detailed experimental benchmark data is essential for theoretical modeling efforts. Ionization of atomic hydrogen by electron or bare ion impact, i.e. a pure three-body system, constitutes a particularly important test case. As this represents the simplest collision system pertaining to the few-body problem, it is most suitable to test the fundamental components of theoretical models. For heavier target atoms, the presence of passive electrons, i.e. those not undergoing a transition in the collision, means that in the calculation a significantly more complex target

wavefunction has to be used for both the initial and the final continuum state. Although to find a sufficiently accurate wavefunction is usually not too problematic, using it in conjunction with a complex scattering amplitude can make the calculation of cross sections numerically much more complicated. As a result, measurements for heavier target atoms may provide a test on the numerical accuracy of the electronic wavefunction, but they are not ideally suited to test the basic description of the reaction dynamics. Since the hydrogenic wavefunction is an exact solution of Schrödinger's equation, collisions involving atomic hydrogen have no ambiguity as to the cause of any inconsistencies between theory and experiment and can provide further detail into the importance of the PT interaction.

Experiments using an atomic hydrogen target are much more challenging than a noble gas or molecular gas target because of the need to efficiently dissociate molecular hydrogen. Although extensive literature exists on total cross section measurements for electron capture [38-40], electron excitation [41,42], and ionization [43-45] of atomic hydrogen [43-45], differential measurements are much rarer [46-52]. Ion impact measurements differential in projectile parameters are particularly difficult because the scattering angle θ_p and the energy loss ΔE (relative to the total energy) are usually very small. The scattering angle resolution needs to be of the order of 0.1 mrad while the relative energy resolution needs to be of the order of 10^{-5} . A simultaneous measurement of both quantities with sufficient resolution is very difficult even for a helium target and has only been accomplished at Missouri S&T using a unique high-resolution projectile energy-loss spectrometer [51,52]. For an atomic hydrogen target, one is confronted with the additional problems associated with the need to dissociate molecular hydrogen and a

much smaller target density compared to helium. Furthermore, because of the imperfect dissociation, the projectiles have to be measured in coincidence with the recoil ions in order to separate H^+ from H_2^+ and from residual-gas background. Because of these difficulties, only single differential cross sections as a function of θ_p for capture [47] and excitation [48] and as a function of ΔE for ionization [49] have been reported. For doubly differential cross sections, experiments have reported atomic hydrogen data as a function of E_e and θ_e for ionization [46-48] and as a function of p^{rec}_{\perp} and $p^{\text{rec}}_{\parallel}$ for capture [52]. Measured data on double differential cross sections (DDCS) as a function of both θ_p and ΔE (or equivalently electron energy) for ionization of atomic hydrogen by ion impact do not exist. Only for electron impact, for which θ_p and ΔE are much easier to measure, experimental multiple differential cross sections as a function of projectile parameters are available [53,54]. However, these measurements are restricted to relatively small projectile energies, where significant differences between the ionization cross sections for electron and ion impact are expected [55,56].

In this dissertation, the first measurements of DDCS as a function of θ_p and ΔE (which will be labeled DDCS_p from this point forward to avoid confusion with other DDCS) for ionization of atomic hydrogen by ion impact were performed. This data represents the most sensitive test case of the theoretical description of the collision dynamics in a pure three-body system currently available for ion impact. The comparison with theory confirms that difficulties of various theoretical models to reproduce earlier experimental data for ionization of helium by ion impact [2] are not just caused by the complexity of the initial target state, but are due to an insufficiently accurate description of the few-body dynamics of the active particles.

2. THEORETICAL MODELS

2.1. OVERVIEW

As previously stated in the introduction, for systems involving three or more mutually-interacting particles, Schrödinger's equation cannot be solved analytically even when the underlying forces are precisely known. Therefore, it is extremely difficult to accurately determine the spatial and temporal evolution of few-body systems. Moreover, even macroscopic systems of three or more bodies (e.g. the solar system), governed by classical mechanics and under the influence of the gravitational force, do not have an exact solution. However, unlike macroscopic systems, the wave-like nature of atomic and sub-atomic, among other difficulties, makes even approximate solutions to microscopic systems extremely arduous.

In the case of single ionization of atomic hydrogen, there are three particles in the exit (postcollision) channel: the projectile (proton), the ejected electron, and the recoil ion (proton). Due to the charge of all three particles, the Coulomb force is acting on all particle pairs (p_1 -e, p_2 -e, p_1 - p_2) within the system. This represents a "pure" three-body system, i.e. the simplest system for which Schrödinger's equation is not analytically solvable. Therefore, single ionization of atomic hydrogen is an ideal test-case for the few-body problem. Such a "pure" three-body system offers a couple of important advantages: 1) the electronic wavefunction is a hydrogenic wavefunction which is an exact solution of Schrödinger's equation, so the initial state of the target atom is completely understood, and 2) the target atom has no passive electron(s) involved in the interaction, so there is no screening of the nuclear charge nor any electron-electron

interaction. Therefore, any discrepancies between theory and experiment can be directly attributed to the description of the reaction dynamics of this most fundamental system.

Due to the complexity of three-body interactions and the fact that the Coulomb force acts between two particles, it is helpful to consider three two-body Coulomb pairs; electron-projectile, electron-target ion, and projectile-target ion. The contribution of each of these pair-wise interactions to the total three-body dynamics as well as the pair's interaction with the third particle is the basis for the theoretical treatment of the few-body problem in atomic collisions.

2.2. CLASSICAL RUTHERFORD SCATTERING

Although Rutherford scattering is a classical description of a quantum mechanical system, neglecting the wave-like nature of atomic particles, it does provide some insight into the collision dynamics and is a good starting point for more complex theoretical treatments. Not only that, Schulz et al. [37] have found that convoluting a quantum mechanical theoretical model, which does not account for the PT interaction, with classical elastic scattering between the projectile and target ion describes out-of-plane scattering with great success (see Introduction). This theoretical model is described in more detail in Section 2.5.

In his groundbreaking paper [1], Rutherford found that the incident particle's scattering angle is dependent on its charge and energy, the target's charge, and the impact parameter (the distance perpendicular to the projectile's initial momentum and the target) by the following relation:

$$b = \frac{Z_1 Z_2}{2E} \cot \frac{\theta}{2} \quad (1)$$

where θ is the scattering angle, Z_1 is the charge of the projectile, Z_2 is the charge of the target, and E is the energy of the projectile. From this relation, one sees a correlation between the impact parameter and the scattering angle which is, in general, true for all collision systems of particles interacting through a r^{-1} central potential, namely, the smaller the impact parameter, the larger the Coulombic interaction and scattering angle. From the collision geometry shown in Figure 2.1, one can see the differential cross section, $d\sigma$ (the shaded area) is:

$$d\sigma = 2\pi b db. \quad (2)$$

The differential cross section as a function of impact parameter, $\frac{d\sigma}{db}$, is directly proportional to the impact parameter. By applying the chain rule to $\frac{d\sigma}{db}$, one can calculate the differential cross section as a function of the projectile solid angle, $\frac{d\sigma}{d\Omega}$:

$$\frac{d\sigma}{d\Omega} \frac{d\Omega}{db} = 2\pi b \quad (3)$$

from Figure 2.1:

$$d\Omega = 2\pi \sin\theta d\theta. \quad (4)$$

By combining (3) and (4), one obtains:

$$\frac{d\sigma}{d\Omega} = \frac{b}{\sin\theta} \left| \frac{db}{d\theta} \right|. \quad (5)$$

Finally, differentiating b with respect to θ , one obtains the differential cross section as a function of the projectile scattering angle:

$$\frac{d\sigma}{d\Omega} = \left(\frac{ZZ'}{2E} \right)^2 \sec^4 \frac{\theta}{2}. \quad (6)$$

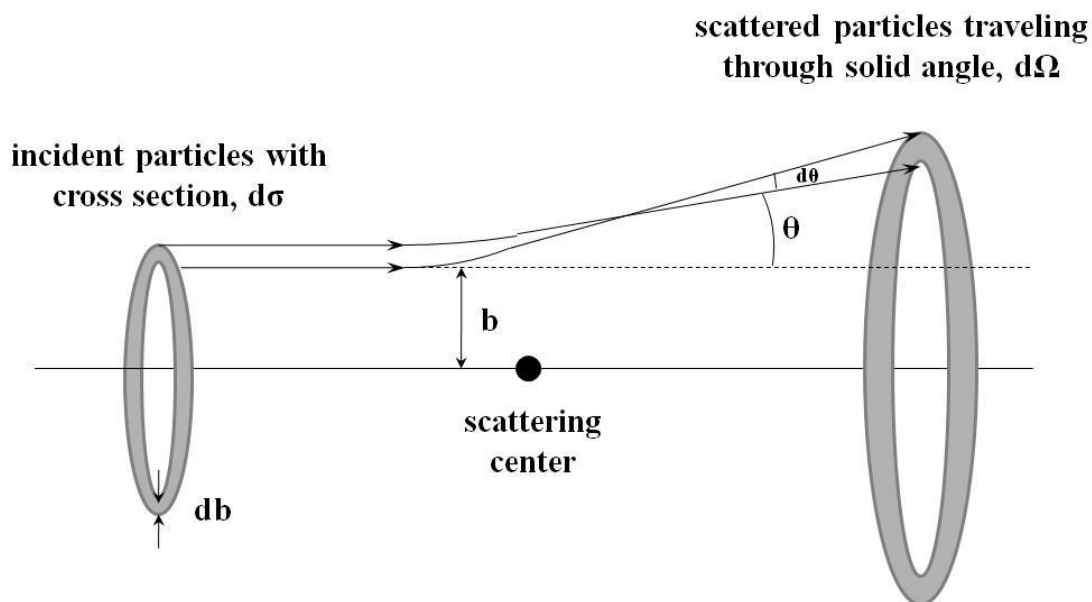


Figure 2.1. An ideal two-body collision system showing the dynamics of Coulomb interaction between two charged particles which leads to the incident particles with an impact parameter, b , being deflected by an angle θ .

2.3. GENERAL CONSIDERATIONS OF QUANTUM MODELS: A PERTURBATIVE APPROACH

Although classical and semi-classical models can provide insight into the mechanisms of atomic interactions, a complete understanding of atomic systems can only be attained by a quantum mechanical model. Therefore, one must solve the Schrödinger equation corresponding to the system's particular Hamiltonian and boundary conditions. This, however, becomes a tedious task since systems of three or more particles do not have an exact analytic solution. To overcome this problem, theorists develop approximations with the goal to accurately describe the dynamics studied in experiments. One type of theoretical approximation, widely used, is the perturbation method where the initial Hamiltonian of the target atom is “disturbed” or perturbed by the projectile through

a “weak” potential relative to the total energy of the system. The potential can be “weak” by either being a relatively large distance between particles or the interaction time of the potential is a very short time.

The general approach to solving Schrödinger’s equation for scattering systems in this section will closely follow the work of Rodberg and Thaler [57]. Atomic units will be used throughout unless otherwise noted, and, for simplification, all calculations are in the center-of-mass reference frame. Also, more complex processes such as ionization and charge transfer involve energy transfers and different potentials in the initial and final state, and therefore, different Hamiltonians. Therefore, an introduction to the general ideas using only elastic collisions will be treated. More complex processes can be solved in a similar fashion as is done in this section and can be found in the references therein.

The time independent Hamiltonian for two interacting particles in a conservative potential $V(\mathbf{r})$ is given by:

$$(E - H_o(\vec{r}))\psi(\vec{r}) = V(\vec{r})\psi(\vec{r}) \quad (7)$$

where E is the energy in the center-of-mass frame, \vec{r} is the relative distance between the two particles, $\psi(\vec{r})$ is the scattered state of the system, and H_o is the unperturbed Hamiltonian of the system given by:

$$H_o(\vec{r}) \equiv -\frac{1}{2\mu}\nabla^2 + V_o(\vec{r}) \quad (8)$$

where μ is the reduced mass, ∇^2 is the Laplacian, and V_o is the initial potential. In a time-independent formulation, the wavefunction of the system can be expressed by the Lippmann-Schwinger equation, which is a solution to the differential equation shown in (7):

$$\psi(\vec{r}) = \chi(\vec{r}) + \int d^3r' G(\vec{r}, \vec{r}') V(\vec{r}') \psi(\vec{r}') \quad (9)$$

where $G(\vec{r}, \vec{r}')$ is the Green's function given by:

$$G(\vec{r}, \vec{r}') = -\left(\frac{2\mu}{4\pi}\right) \frac{e^{ik|\vec{r}-\vec{r}'|}}{|\vec{r}-\vec{r}'|} \quad (10)$$

and $\chi(\vec{r})$ (unperturbed state) is the solution for $V(\vec{r}) = 0$. If $V_0(\vec{r}) = 0$, then $\chi(\vec{r})$ is simply a plane wave. In bra-ket notation, the Lippmann-Schwinger equation is:

$$|\psi\rangle = |\chi\rangle + GV|\psi\rangle. \quad (11)$$

By iteratively replacing $|\psi\rangle$ on the right hand side of (10) by $|\psi\rangle$ on the left hand side of (10), one obtains an approximation for the exact perturbed state $|\psi\rangle$ in terms of the unperturbed state ($V(\vec{r}) = 0$), $|\chi\rangle$, in powers of the potential, V :

$$|\psi\rangle = |\chi\rangle + GV[|\chi\rangle + GV|\psi\rangle]. \quad (12)$$

In general,

$$|\psi\rangle = \sum_{n=0}^{\infty} (GV)^n |\chi\rangle. \quad (13)$$

This is known as the Born Expansion and truncating the series after the n^{th} term is referred to as the n^{th} order Born approximation.

The differential cross section, $\frac{d\sigma}{d\Omega}$, for a given system is related to the potential by the scattering amplitude, $f(\theta, \varphi)$ by:

$$\frac{d\sigma}{d\Omega} = |f(\theta, \varphi)|^2 \quad (14)$$

$$f(\theta, \varphi) = -\frac{\mu}{2\pi} \langle \chi_{k_f} | V | \psi \rangle \quad (15)$$

where $\langle \chi_k |$ is the scattered particle in a continuum state. Since $|\psi\rangle$ is an energy eigenstate of the total Hamiltonian, H , it is somewhat easier to consider unperturbed

initial state wavefunction dependent only on the initial wavevector, k_i . This is made possible with the T operator, which relates χ_{k_i} to ψ_i :

$$T = V + V \frac{1}{E-H+i\epsilon} V \quad (16)$$

where:

$$T|\chi_{k_i}\rangle = V|\psi_i\rangle \quad (17)$$

and ϵ is an infinitesimal. The ‘‘T-Matrix’’ or transition amplitude describes the change from the initial state, χ_{k_i} , to the final state, χ_{k_f} , in matrix form:

$$\langle T \rangle = \langle \chi_{k_f} | T | \chi_{k_i} \rangle = \langle \chi_{k_f} | V | \psi_i \rangle \quad (18)$$

and is related to the differential cross section by:

$$\frac{d\sigma}{d\Omega} = \left(\frac{\mu}{2\pi}\right)^2 |\langle T \rangle|^2. \quad (19)$$

For more complex processes, such as ionization, the multiplicative factor in (19) changes. However, the relation between the T-Matrix and the differential cross section remains the same.

For single ionization of atomic hydrogen, the fully differential cross section, originally derived by Bethe [58], presented in the form given by Madison et al. [19] is:

$$\frac{d\sigma^3}{d\Omega_p d\Omega_e dE_e} = (2\pi)^4 \mu_{Te} \mu_{PA}^2 \frac{k_f k_e}{k_i} |\langle T \rangle|^2 \quad (20)$$

where Ω_p is the solid angle of the scattered projectile, Ω_e is the solid angle of the ejected electron, E_e is the ejected electron’s energy, μ_{Te} is the reduced mass of the target atom (≈ 1), μ_{PA} is the reduced mass of the atom and projectile, k_f is the final momentum of the projectile, k_i is the initial momentum of the projectile, and k_e is the electron’s momentum. By integrating over the electron solid angle, $d\Omega_e$, in (20), one obtains a DDSCS_p as

measured in this dissertation. The full and unperturbed Hamiltonians for this system are given by:

$$H = T_p + T_e + V_{pT} + V_{pe} + V_{eT} \quad (21)$$

$$H_o = T_p + T_e + V_{eT} \quad (22)$$

where T_p is the kinetic energy of the projectile, T_e is the kinetic energy of the electron, V_{pT} is the interaction potential between the projectile and target ion, V_{pe} is the interaction potential between the projectile and electron, and V_{eT} is the interaction potential between the electron and target ion. The difference of the full Hamiltonian and unperturbed Hamiltonian, i.e. the perturbing potential, is given by V_{pe} and V_{pT} .

The ensuing theoretical models are discussed solely on their treatment of the various particle interactions and the particle's wavefunction without going into the mathematical subtleties of each model. The differences between theories will be discussed based on the physics described and whether the specific theoretical approximations are appropriate for the situation it describes. For a much more in-depth look into the various theories, it would be best to review the cited sources.

2.4 FIRST AND SECOND BORN APPROXIMATIONS

As stated earlier, First Born Approximation (FBA) differential cross sections were initially derived for atomic collisions systems by Bethe [58] (further review article by Inokuti [59]) and the first FBA DDCS for proton impact (on a Helium target) was calculated by Oldham [60,61]. The First Born Approximation is the first term in the Born expansion where the initial state is treated as an unperturbed state. The T-Matrix for the FBA is then:

$$\langle T \rangle^{FBA} = \langle \chi_{k_f} | V | \chi_{k_i} \rangle. \quad (23)$$

The projectile is treated as a plane wave in both the initial and final state with different wavevectors dependent on the momentum transferred to the target atom. The target electron is treated as an eigenstate (ground state) wavefunction in the initial state and a continuum eigenstate wavefunction in the final state. Although the projectile-target nucleus interaction (PT) is formally included in the Hamiltonian, it does not play a role in the calculation of the T-Matrix due to the orthogonality of the electronic wavefunctions. The FBA essentially treats the ionization as a first order process meaning it only accounts for the initial interaction between the electron (leading to ejection) and the projectile. It does not account for higher order processes such as the PT interaction or secondary electron interactions with the projectile [61] (i.e. the FBA only accounts for direct transitions from the ground state to the final continuum state). Although the FBA has well reproduced total cross sections for atomic systems as early as the work of Bates and Griffing [62], discrepancies were observed at both large and small electron scattering angles in differential cross sections [61]. The discrepancies at large scattering angles were improved by Madison [63] with the use of a Hartree-Fock potential to account for the passive electrons in the target atom, but the discrepancies at small scattering angles remained. Undoubtedly, for multiple differential measurements such as FDCS, which provide a much more stringent test to theoretical models, the problems of the FBA are only further illustrated [26]. That being said, the FBA does provide a means of comparison to more elaborate models, such as distorted and Coulomb wave models (see Sections 2.5 and 2.7), and useful information on the relative importance of the first order ionization process in a collision system.

The Second Born Approximation (SBA), taking the Born expansion (13) to the second term, accounts for higher order processes that are left out of the FBA. This is accomplished by adding an intermediate step between the electronic transition from the ground state to the continuum. The T-Matrix in the SBA is given by:

$$\langle T \rangle^{SBA} = \langle \chi_{k_f} | V | \chi_{k_i} \rangle + \langle \chi_{k_f} | V G V | \chi_{k_i} \rangle. \quad (24)$$

The Green's function contains the intermediate state of the system after the primary interaction. This intermediate state can involve an electronic or projectile state that is different from its respective initial state. If the intermediate electronic state is different from its initial state, from a physical perspective, the electron, initially in the ground state, is brought to an excited state by the initial interaction with the projectile and is then further excited to the continuum through a secondary interaction with the projectile. As in the FBA, the PT interaction has then no effect on the cross sections due to the orthogonality between the initial and intermediate state. On the other hand, if the electronic intermediate state is identical to the initial state (i.e. the electron stays in the ground state) and only the projectile intermediate state differs from the initial state, then the PT interaction contributes to the cross section in terms of elastic scattering.

The condition for the Born approximation to hold is that either the interaction is sufficiently weak and/or the interaction time is small enough not to have a large effect on the overall energy of the system [64]. For charged particle Coulomb interactions, this can be stated as the projectile charge-to-velocity ratio (known as the perturbation parameter, η) must be much less than 1.

2.5 CONTINUUM DISTORTED WAVE-EIKONAL INITIAL STATE MODEL

Another possibility to treat the physics of higher order contributions is to include the interactions in the wavefunctions themselves. One such approach is the Continuum Distorted Wave Approximation (CDW). In the CDW model, initially developed by Chesire [66] for electron capture and further applied to ionization by Belkic [67], the initial bound electron wavefunction is distorted by the presence of the projectile and the final continuum electron wavefunction is distorted by both the projectile and the target ion. It was pointed out by Crothers et al. [68] that the distorted wave in the initial state does not satisfy the boundary conditions, which resulted in significant discrepancies to experimental data. In order to address this problem, Crothers et al. [68] developed the Continuum Distorted Wave-Eikonal Initial State Approximation (CDW-EIS), which replaces the initial distorted wave by its Eikonal approximation. This is considered to be a semi-classical approximation since the initial projectile is approximated to travel in a straight line with respect to the target atom at a fixed impact parameter, b , which is the perpendicular distance between the projectile's initial trajectory and the target atom. The Eikonal phase is obtained from a Fourier transformation of the b -dependent transition amplitude.

A main difference between the CDW-EIS and FBA, besides the choice of wavefunctions, is the treatment of the perturbing potential. In the CDW model and, similarly, in the CDW-EIS model with slightly different wavefunction (see Fainstein et al.[69]), the perturbing potential, V , is broken into two parts: the distorting potential, U , and the associated potential, W , where:

$$V = U + W. \quad (25)$$

The distorting potential, U , is chosen such that it contains the behavior of the long-range Coulomb potential [69]. The distorted wavefunction, Ψ^{CDW} , is then chosen to give an exact solution to the Hamiltonian which includes U :

$$(H_0 + U)\Psi^{CDW} = E^{CDW}\Psi^{CDW}. \quad (26)$$

The T matrix is then solved with the remaining potential, W , and the wavefunction, Ψ^{cdw} where W is considered weaker than the distorting potential, V , in the Born approximation, and therefore, the series will converge faster [70]. The CDW-EIS T-Matrix is then:

$$\langle T \rangle = \langle \Psi^{CDW} | W | \Psi^{EIS} \rangle \quad (27)$$

where Ψ^{EIS} is the Eikonal Initial State wavefunction.

The CDW-EIS model is a drastic qualitative improvement to the FBA models due to its treatment of higher order processes; however, quantitatively, there are still discrepancies between theory and experiment [69]. The CDW-EIS is still afflicted with several shortcomings: 1) as mentioned above, the PT interaction is not treated fully quantum mechanically, but semi-classically. 2) In terms of the electron, it represents a 2-state approximation (i.e. a transition from the ground state to one specific continuum state). Therefore, the presence of other reaction channels (e.g. electron excitation or capture) are completely ignored. This results in an incorrect normalization of the wavefunction. 3) Effectively, the CDW-EIS model breaks the 3-particle system up in three independent 2-particle subsystems. The missing correlation between the various particle pairs means that Ψ^{CDW} is only accurate if at least one particle is well separated from the other two particles.

2.6 FBA CONVOLUTED WITH CLASSICAL ELASTIC SCATTERING OF THE PT INTERACTION

Convoluting classical elastic scattering with the FBA (or any other model which excludes the PT interaction; in this dissertation, a version of the CDW-EIS was used) is a means of combining a more complex quantum mechanical theory with a simple, classical approach to the PT interaction. On a broader scale, it allows for a better understanding of the physical significance of a particular interaction that is not so well understood by more complex theories. This particular method was introduced by Schulz et al. [37] to better understand the cause of the structure seen in the perpendicular plane of single ionization of He by C^{6+} impact [2] (see Figure 1.3 for results). A similar method can be used to convolute experimental resolution into a theoretical model as shown by Dürr et al. [36]. This section will closely follow the work of Schulz et al [37].

To accomplish the aforementioned convolution, a Monte Carlo event generator (MCEG) method was used to add event-by-event the projectile momentum transfer and target ion momentum from the PT interaction to the previous momentum due to the projectile and target ion interacting with the ejected electron calculated with the FBA. Classically, the momentum transfer, q_{es} , is given by the following relation:

$$q_{es} = \frac{2Z_1Z_2}{bv_o} \quad (28)$$

where Z_1 and Z_2 are the projectile and target nuclear charge, respectively, b is the impact parameter, and v_o is the projectile speed. For a Helium target, which was the target used by Schulz et al. [37], the impact parameter dependent effective target nuclear charge was calculated using a parametrization which represents a good fit to a Hartree-Fock potential. Therefore, the momentum transfer from elastic scattering is, for a given

system, fully determined, by the impact parameter. The impact parameter distribution was calculated using two sets of uniform random number distributions and a set of equations (see [37]) determined partly by trial-and-error and partly by analytical means. This distribution, $bP(b)$, where $P(b)$ is the ionization probability for a given impact parameter, was then fit to a theoretically-calculated $bP(b)$. The magnitude of q_{es} for a given event is then calculated using (28). The direction of q_{es} is determined by a separate uniform random number distribution between 0 and 2π . The momentum transfer from q_{es} is then added event-by-event to the projectile and target ion momentum previously calculated through the FBA model. The new momentum distributions are then analyzed to create new FDCS.

Although this method produces very good agreement to experimental data [37,71], it does not provide a complete theoretical picture of the ionization dynamics. The obvious disadvantage is that the PT interaction is treated in terms of pure classical mechanics. Since atomic collisions obviously represent quantum mechanical systems, a complete understanding can only be obtained if fully quantum mechanical calculations can consistently reproduce experimental data.

2.7 THREE COULOMB WAVE MODEL

Similar to the distorted wave models in the Three Coulomb Wave Model (3C) the final wavefunction is distorted due to interactions between the three free particles. Initially developed by Godunov et al. [72,73] for proton impact with further work by Brauner et al. [74] for electron impact, the 3C model modifies the final state wavefunction of the FBA by multiplying it by two Coulomb distortion factors

corresponding to the projectile-electron and projectile-target nucleus pairs. Since the ejected electron is given by a Coulomb wave already in the FBA, the final state wavefunction in this model is a product of three Coulomb waves, thus the name 3C. The 3C T-Matrix is given by:

$$\langle T \rangle = \langle \chi_{kf} C_{PT} C_{Pe} C_{eT} | V | \chi_{ki}^{FBA} \rangle \quad (29)$$

where C_{ij} is the Coulomb distortion factor for each Coulomb pair and χ_{kf} is the projectile plane wave. Similar to the CDW-EIS model, 3C, too, ignores the correlation between the various particle pairs. By this approximation, at least one of the three particles should be well-separated from the other two particle subsystem. This puts a limitation on the system parameters for which this approximation would be valid. However, Godunov et al. [75] found that in areas where the 3C approximation holds; there is good agreement between theory and experiment. Furthermore, the 3C model treats all three interactions to the same order corresponding to the exact Coulomb boundary conditions [74].

3. EXPERIMENTAL SETUP

3.1 OVERVIEW

Kinematically complete information of an event such as single ionization involves attaining the three dimensional momentum vectors of all particles involved in the event. In the case of single ionization of atomic hydrogen by proton impact, there are only three particles involved in the collision process: the projectile proton, the ejected electron, and the target proton. Only two of the three momentum vectors have to be measured directly since the third momentum vector can be deduced from the conservation of momentum. Therefore, there are three possible combinations of measurements to perform a kinematically complete experiment of single ionization: measuring the momentum-analyzed projectiles and target ions in coincidence, measuring momentum-analyzed target ions and ejected electrons in coincidence, or measuring the momentum-analyzed projectiles and ejected electrons in coincidence. The PROjectile + Target Ion Momentum Spectrometer (PROTIMS) at the Missouri University of Science & Technology uses the first method of measuring the momentum-analyzed projectiles and target ions in coincidence to gain the complete kinematics of few-body collisions such as single ionization.

The Ion-Energy Loss Spectrometer was initially designed by John Park [76] in the 1960s. In the 1990s, a recoil ion momentum spectrometer using a cold target beam (COLTRIMS) [12,13] was added along with position-sensitive detectors in order to obtain fully differential measurements of various three-body collision systems. Also, a 45° parallel plate energy analyzer [77] replaced the former hemispherical energy

analyzer. The most recent addition to the experiment, implemented as part of the project outlined in this thesis, is a new cooled jet based on a microwave discharge dissociator designed to create an atomic hydrogen beam.

An overhead diagram of the experimental layout is shown in Figure 3.1 while a more detailed schematic of the projectile + target ion momentum spectrometer is shown in Figure 3.2. A 5 keV proton beam is initially produced using a hot cathode ion source. The protons are then accelerated to 75 keV and collimated to a cross sectional size of approximately 0.02 mm^2 . Next, the projectile proton beam intersects with a cold atomic hydrogen target beam produced using a microwave dissociator. The atomic hydrogen recoil ions produced from the collision are then momentum-analyzed and detected by a position-sensitive detector. The scattered projectiles are decelerated by 70 keV and then pass through a 45° parallel plate electrostatic energy analyzer where the energy loss from the collision is measured and, finally, the projectile scattering angle is measured using another position-sensitive detector. The projectile scattering angle along with its energy loss gives the projectile momentum. Measuring the projectile momentum in coincidence with the recoil ion momentum constitutes kinematically complete information.

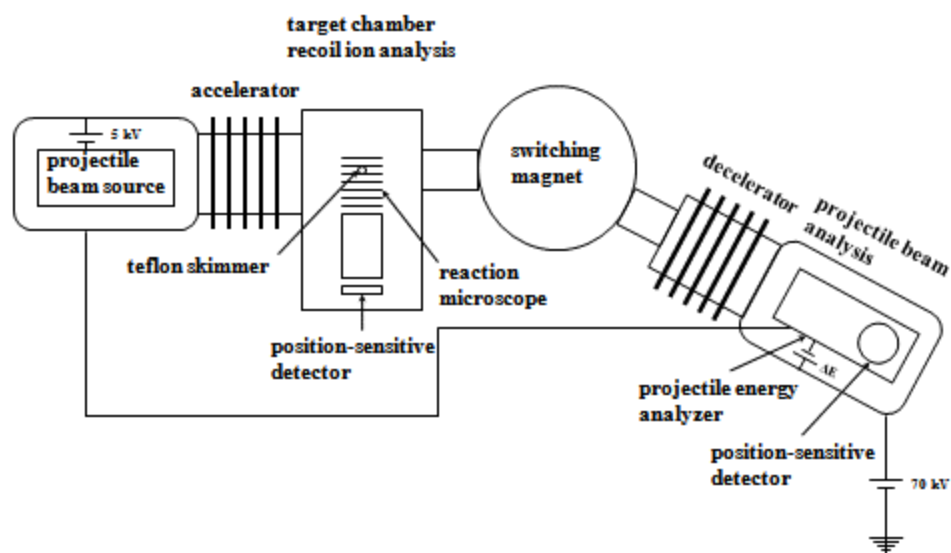


Figure 3.1. Overhead experimental layout for the PROjectile + Target Ion Momentum Spectrometer (PROTIMS).

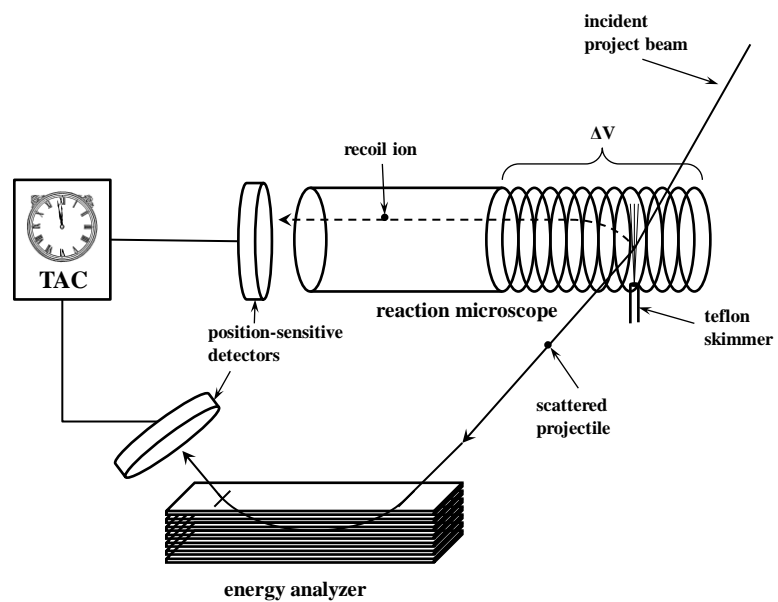


Figure 3.2. Schematic for kinematically complete experiment on single ionization.

As briefly stated in the introduction, kinematically complete data for ionization by ion impact is extremely difficult to obtain. First, the scattering angle of an ion projectile, as compared to an electron projectile, is immensely smaller with the exception of very slow projectiles. An ion's scattering angle is typically only a fraction of a milliradian or one-hundredth of a degree, whereas, electron scattering angles of tens of degrees are not unusual. Therefore, to obtain meaningful results, a projectile scattering angle resolution of approximately 0.1 mrad is necessary. An even more challenging requirement is the projectile energy loss resolution. Due to the large mass difference, it takes approximately 2000 times more energy for a light ion like a proton to even have the same speed as an electron. For 75 keV protons, an intermediate energy projectile, it takes a relative energy resolution, $\frac{\delta E}{E}$, of the order of 10^{-5} to attain an overall energy resolution of approximately 1 eV. Currently, the projectile momentum spectrometer at Missouri S&T is the only apparatus, worldwide, that achieves both the projectile angular and energy loss resolution stated above, thanks to the unique accelerator-decelerator feature (see Section 3.3).

The recoil ion momentum needs to be measured in coincidence (see Section 4.2) with the projectile ion momentum to ensure that the detected recoil ions and projectiles originate from the same ionization event. Only then can the electron momentum be deduced from momentum conservation. Furthermore, coincidence measurements are needed to separate ionization of atomic hydrogen from undissociated molecular hydrogen and residual gases. As a result of the limited detection efficiencies, only a small fraction of all ionization events are recorded as valid coincidences. A further difficulty is posed by the requirement to dissociate molecular hydrogen. Microwave radiation, which was used to dissociate molecular hydrogen, increases the average temperature of the target

gas considerably. However, to obtain fully differential measurements, a cold target gas of a few Kelvin is required. Therefore, the heating of the target gas to produce atomic hydrogen is counterproductive to the need of producing a cold target gas. These difficulties explain the very limited experimental differential data currently available for ionization of atomic hydrogen by ion impact (see Section 1). Due to the difficulty, the kinematically complete experiment, on which this dissertation is based, was only able to attain doubly-differential cross sections as a function of the projectile solid angle, Ω_p , and energy loss, ΔE . That being said, the data presented in this dissertation is, nevertheless, the most sophisticated experiment, to date, on ionization of atomic hydrogen by ion impact.

3.2 PROJECTILE BEAM SOURCE AND ACCELERATOR

The proton beam is initially created using a hot cathode ion source manufactured by Colutron Research Corp. in Boulder, Co. A schematic of the ion source is shown in Figure 3.3. A 3:1 gas mixture of H_2 to Ar is pumped into the ion source with a variable leak valve. The cathode filament, operated at 12 V and 16 A, produces primary electrons, which ionize the gas mixture. The inert Ar gas serves as a source of a large number of electrons (8 valence electrons per atom). The primary electrons undergo further collisions with the source gas producing a large number of secondary electrons so that a self-sustaining plasma discharge is created. The anode is held at a constant voltage of 75 V. This bias, known as “reverse-biasing”, causes all ions besides those very close to the anode to be accelerated away from the extraction field. With this biasing, the influence of the spatial variations of the plasma potential on the extracted beam energy spread is minimized. As a result, the overall energy spread of the extracted beam is much

less than 1eV [77]. The extraction field then gives the extracted ion beam an energy of 5 keV.

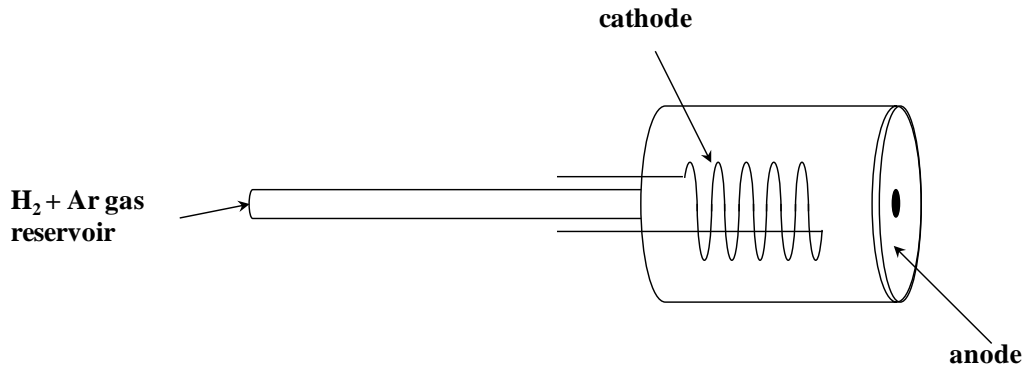


Figure 3.3. Schematic of ion beam source.

At this point, the ion beam consists of H^+ , H_2^+ , H_3^+ , and multiple charge states of Ar. The next step is to filter out all unwanted ion species thereby creating a homogenous beam of ions with the same energy. First, the unfiltered ion beam is focused using an electrostatic Einzel lens. The focused beam then passes through a Wien filter [78], which consists of orthogonal electric and magnetic fields that separate ions based upon their charge-to-mass ratio, q/m . Ions extracted with a specific potential, V_{ext} , have a velocity proportional to the square root of its charge-to-mass ratio.

$$\frac{1}{2}mv^2 = qV_{ext} \quad (30)$$

$$\Rightarrow v \propto \sqrt{\frac{q}{m}} \quad (31)$$

The force of electric and magnetic fields is given by the Lorentz force law:

$$\vec{F} = q(\vec{E} + \vec{v} \times \vec{B}). \quad (32)$$

If the force due to the electric field and the force due to the magnetic field are in opposite directions, it is possible, for a particle with a specific charge-to-mass ratio, to set the magnitude of both forces equal to one another making the net force equal to zero. All other particles with different charge-to-mass ratios are deflected from the beamline due to the net force not being equal to zero. As is seen in Figure 3.4, the Wien filter “filters” all unwanted particles, thus, creating a pure beam of protons with an energy of 5 keV.

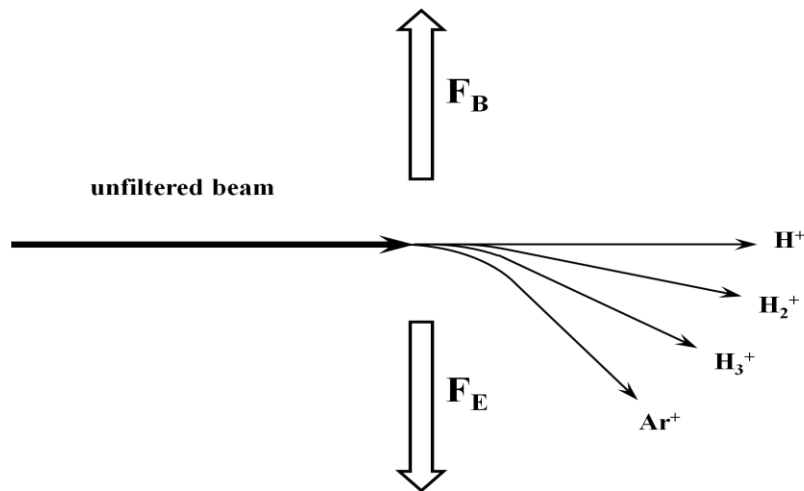


Figure 3.4. Force diagram and relative trajectories of various ion species dependent on the ion’s charge-to-mass ratio.

Next, the 5 keV proton beam is accelerated to 75 keV by a uniform electric field generated by a series of electrodes connected to one another by a resistor chain. The

beam is then collimated by a set of perpendicular slits of width 0.15 mm which gives the beam a cross sectional size of 0.02 mm^2 . The proton beam now enters the target chamber where it intersects with the target beam.

3.3 SWITCHING MAGNET AND DECELERATOR

After the target chamber and the resulting collision event, the scattered projectiles travel through a switching magnet which deflects the projectile beam 30° from its original direction. As in the Wien filter, the switching magnet acts as a “filter” assuring that only protons reach the decelerator and are eventually momentum-analyzed while charge-exchanged beam components (neutral H) go straight through the magnet.

The non-charge-exchanged projectiles passing the switching magnet had to be energy-analyzed. The relative energy resolution, $\frac{\delta E}{E}$, of an electrostatic energy analyzer is only dependent on the geometry of the analyzer (see Section 3.4). Therefore, the absolute resolution, δE , is improved by decreasing the total pass energy, E in the analyzer. For that reason, the proton beam is decelerated after passing through the switching magnet and before entering the energy analyzer by floating the terminal in which the analyzer is located to a voltage $V_{\text{dec}} = 70 \text{ kV}$. At this stage, however, a particular proton's energy is dependent on its energy loss, ΔE , due to the interaction with the target atom. To account for this and measure the energy loss at the energy analyzer, the decelerator has an additional power supply floating on the decelerator potential. As shown in Figure 3.1, the output of this power supply relative to the decelerator is ΔV , i.e. $70 \text{ kV} + \Delta V$ relative to the laboratory ground. The output voltage ($70 \text{ kV} + \Delta V$) is

connected to the accelerator terminal. Therefore, the proton energy after acceleration, but before the collision, is given by

$$E_{acc} = qV_{ext} + qV_{dec} \quad (33)$$

The proton energy after deceleration, E_{dec} is then:

$$E_{dec} = qV_{ext} + q\Delta V - \Delta E \quad (34)$$

where q is the charge of the projectile and V_{ext} is the initial extraction voltage of the proton beam at the beam source [76]. For ΔE equal to $q\Delta V$, the proton energy after deceleration is, then, equal to the initial extraction energy of the proton beam (5 keV). The energy loss is thus determined by keeping the spectrometer voltage fixed corresponding to a pass energy of 5 keV and setting ΔV equal to $\Delta E/q$. By sharing the same power supply, one avoids any complications from voltage fluctuations between the accelerator and decelerator. For 75 kV, the current power supply can have voltage fluctuations as large as 15 V. Voltage fluctuations of that magnitude would completely destroy the energy resolution. However, by sharing the same power supply, the fluctuations of the accelerator voltage are compensated by equivalent decelerator voltage fluctuations. It should also be noted that these voltage fluctuations have a negligible effect on the overall projectile beam energy in the collision region since 15 eV is only 0.02% of the total energy.

3.4 PROJECTILE MOMENTUM SPECTROMETER

The unique projectile momentum spectrometer used at Missouri S&T measures the projectile momentum in terms of spherical coordinates: the magnitude of the

projectile's momentum is determined by the energy loss, ΔE , set by the decelerator offset power supply as described in the previous section, the azimuthal angle is fixed by the energy analyzer ($\phi_p = 0$), and the polar angle is measured on a position-sensitive detector (see Section 3.7.1) after the energy analyzer.

The projectile's energy loss is measured using a 45° electrostatic parallel-plate energy analyzer as seen in Figure 3.5. An entrance and exit slit, $75 \mu\text{m}$ in width and 3 cm in length, are cut into the front plate of the analyzer. A constant positive voltage is applied to the back plate of the spectrometer while the front plate is held at ground which produces a uniform electric field inside the spectrometer. The incoming protons will, therefore, follow a parabolic trajectory whose slope is dependent on the initial projectile energy. Only protons with a well-defined energy will pass through the exit slit. If the projectile energy is too large, the trajectory will be above the exit slit and if the projectile energy is too small, the trajectory will be below the exit slit (see Figure 3.5). The spectrometer voltage is related to the pass energy by:

$$\frac{qV}{E} = \frac{2d}{l} \quad (35)$$

where V ($=3.5 \text{ kV}$) is the spectrometer voltage, E ($=5 \text{ keV}$) is the pass energy of the incoming projectiles, d ($=12.3 \text{ cm}$) is the separation between the front and back plate of the spectrometer, and l ($=35.6 \text{ cm}$) is the separation between the entrance and exit slits.

The energy resolution, δE , is given by:

$$\frac{\delta E}{E} = \frac{2w}{l} + 2(\Delta\alpha)^2 + (\Delta\beta)^2 \quad (36)$$

where w is the width of the slit, $\Delta\alpha$ is the acceptance angle of the analyzer in the plane of deflection, and $\Delta\beta$ is the acceptance angle of the analyzer in the plane perpendicular to deflection [77]. In the case of the energy analyzer used in this particular experiment,

$(\Delta\alpha)^2$ and $(\Delta\beta)^2$ are both of the order of 10^{-9} rad², while w/l is of the order of 10^{-4} . Therefore, to a good approximation, the energy resolution is only dependent on the slit width, slit separation, and incident energy. The theoretical resolution for a 5 keV incident beam is 2.1 eV full width at half maximum (FWHM). The experimental resolution for a 2 keV incident beam was measured to be 1.2 eV FWHM and for a 5 keV incident beam about 3 eV FWHM [77].

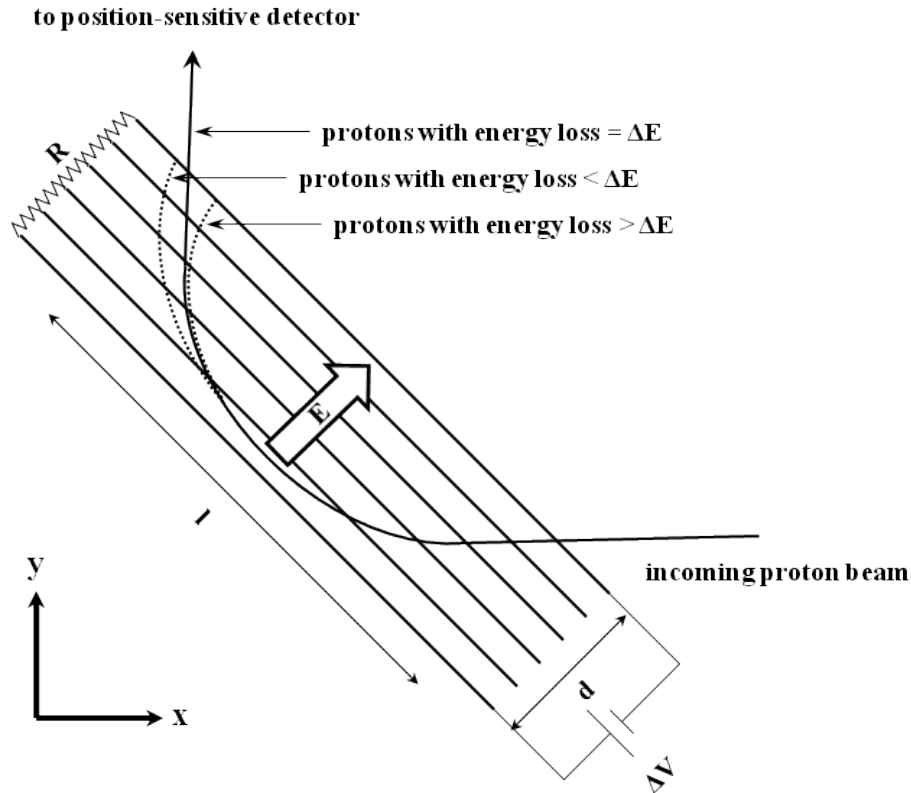


Figure 3.5. Schematic of 45° parallel-plate energy analyzer with relative trajectories dependent on the proton energy loss.

After the energy analyzer, the energy-resolved protons hit a position-sensitive detector where their scattering angle is measured. In terms of momentum, it is common practice to describe the projectile's momentum in terms to the amount transferred to the target atom through the collision. The momentum transfer \mathbf{q} is simply the difference in the initial projectile momentum \mathbf{p}_o and the final projectile momentum \mathbf{p}_f , i.e. $\mathbf{q} = \mathbf{p}_o - \mathbf{p}_f$. The vector relationship of \mathbf{p}_o , \mathbf{p}_f , and \mathbf{q} is shown in Figure 3.6. The components of \mathbf{q} , q_{\parallel} (parallel to \mathbf{p}_o) and q_{\perp} (perpendicular to \mathbf{p}_o), can be related to the energy loss ΔE and the scattering angle θ_p through the following relation:

$$\Delta E = \Delta E_{\parallel} + \Delta E_{\perp} \quad (37)$$

$$\Delta E_{\perp} = E_{f\perp} = \frac{p_{f\perp}^2 \sin^2(\theta_p)}{2m} < 0.1 \text{ eV} \quad (38)$$

for $\theta_p < 1 \text{ mrad}$ (a relatively large angle)

$$\Delta E_{\perp} \approx 0 \quad (39)$$

$$\Rightarrow \Delta E \approx \Delta E_{\parallel} \quad (40)$$

$$\Delta E_{\parallel} = \frac{p_o^2}{2m} - \frac{p_{f\parallel}^2}{2m} \quad (41)$$

$$= \frac{1}{2m} (p_o - p_{f\parallel})(p_o + p_{f\parallel}) \quad (42)$$

$$= \frac{1}{2m} (q_{\parallel})(p_o + p_{f\parallel}) \quad (43)$$

since $q_{\parallel} \ll p_o$

$$\approx \frac{1}{2m} (q_{\parallel})(2p_o) \quad (44)$$

$$= q_{\parallel} v_o \quad (45)$$

where v_o is the initial velocity of the projectile beam

$$\therefore q_{\parallel} \approx \frac{\Delta E}{v_o}. \quad (46)$$

The transverse component of q is given by:

$$\tan \theta_p = \frac{q_{\perp}}{p_o - q_{\parallel}} \quad (47)$$

since $q_{\parallel} \ll p_o$

$$\approx \frac{q_{\perp}}{p_o} \quad (48)$$

since $\theta_p \ll 1$

$$\tan \theta_p \approx \theta_p \quad (49)$$

$$\therefore q_{\perp} \approx p_o \theta_p. \quad (50)$$

Measuring the projectile momentum in coincidence with the recoil ion momentum gives a kinematically complete description of a single ionization collision system.

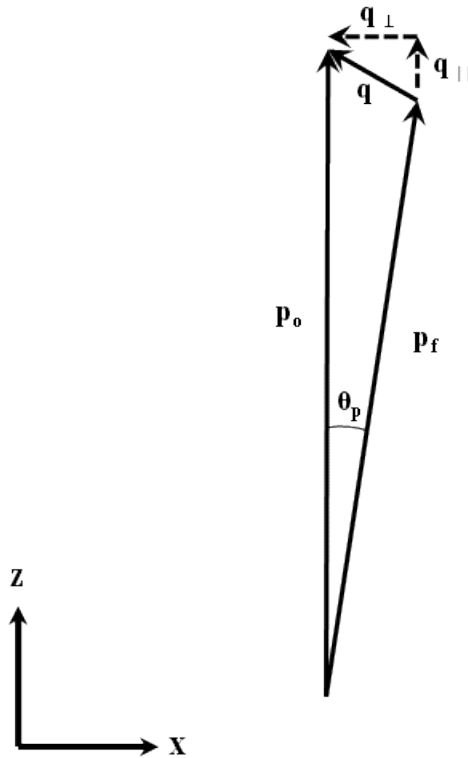


Figure 3.6. Vector diagram of \mathbf{p}_o , \mathbf{p}_f , and $\mathbf{q}(=\mathbf{p}_o - \mathbf{p}_f)$.

3.5 TARGET BEAM PRODUCTION

In order to produce an atomic hydrogen target beam, it is necessary to dissociate molecular hydrogen. This was achieved using a microwave discharge and using Teflon tubing to transport the gas to the target region as described by Paolini et al. [79]. The justification for this method of dissociation is that it is not only feasible to implement to the existing vacuum system, but it is also capable of creating a high enough output of atomic hydrogen to produce supersonic jet. An overall schematic of the target gas handling system is shown in Figure 3.7.

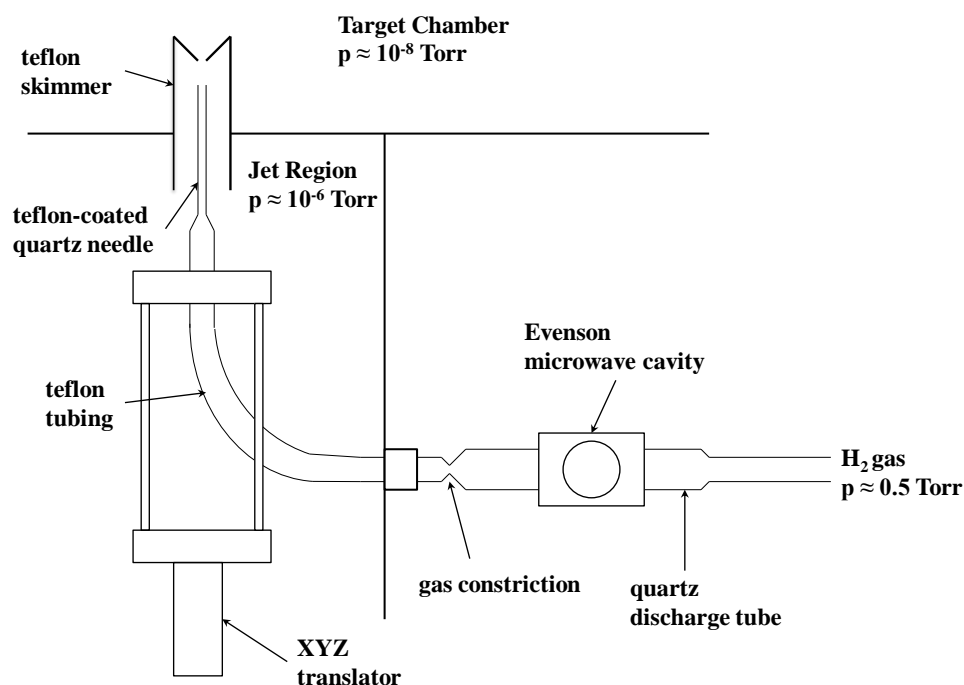


Figure 3.7. Schematic of the jet region including gas handling system and microwave dissociator.

Ultra-pure (99.9995% pure) H_2 gas is pumped into a quartz discharge tube (10mm ID) via a variable leak valve with a constant pressure around 500mTorr. An Evenson microwave cavity, resonantly tuned to the frequency of the microwave field (2450 MHz), operating at around 50 forward watts and 1-2 reflected watts, excites the hydrogen molecules causing some of the molecules to dissociate and/or ionize, thus, creating atomic hydrogen and H_2^+ . Other mechanisms for H production are: the absorption of photons by primary electrons until they gain enough energy to further dissociate and ionize H_2 gas. Also, excited hydrogen ($n \geq 2$) can further excite and dissociate the background H_2 leading to a greater concentration of atomic hydrogen, while ground state hydrogen ($n = 1$) has no recombination channel in a background of H_2 [79]. In order to maintain a stable discharge, a gas constriction, which restricts bulk gas flow, was placed on the exit end of the discharge tube. The gas is transported from the discharge tube by FEP Teflon tubing, which strongly suppresses the recombination of atomic hydrogen at the tubing walls. The Teflon tubing is coupled to a quartz needle, 1 mm inner diameter and 20 mm in length, which was coated with a 40% aqueous dispersion of FEP Teflon manufactured by Du Pont. The needle is mounted to an XYZ translator in order to optimize its overlap with the projectile beam.

As the gas exits the needle, if the pressure ratio between the higher driving pressure of the gas mixture, P_o , and the lower background pressure of the jet chamber, P_b , is greater than, or equal to, 2.1 [80], the bulk gas velocity reaches supersonic speeds. Figure 3.8 shows the gas dynamics in the region of expansion.

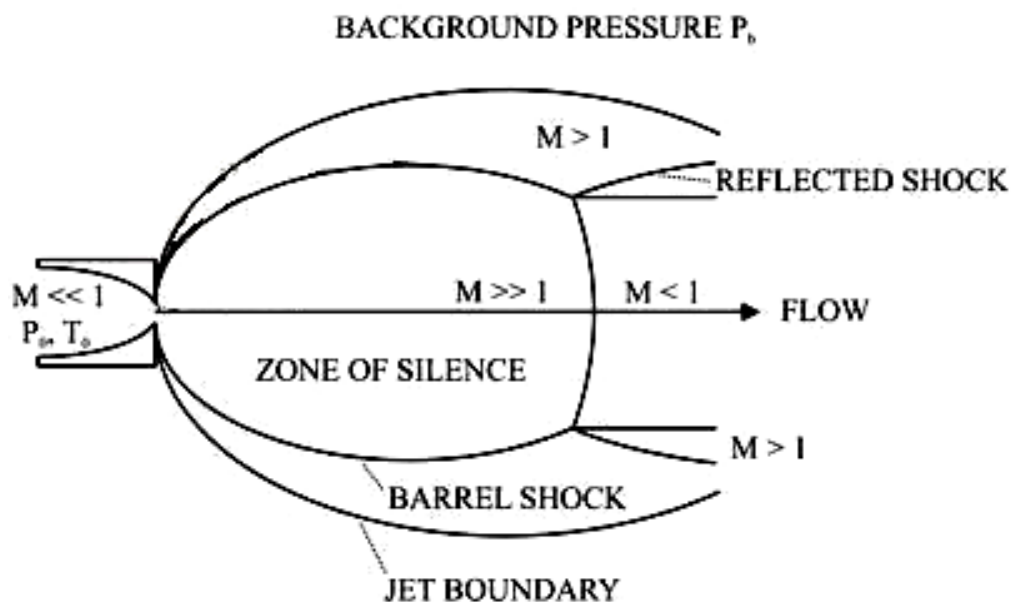


Figure 3.8. Dynamics of gas expansion between two boundaries. The average speed of the gas is given relative to Mach speed, M . The supersonic expansion, $M \gg 1$, creates shockwaves at the boundaries of expansion[80].

During the expansion process, the gas undergoes adiabatic cooling where the thermal motion is transferred to directional motion in the direction of the pressure gradient and the gas temperature in the “zone of silence” reaches around 1-2 K for He [36]. Since, in this particular experiment, the discharge limits the maximum pressure to about 0.5 Torr as well as increases the initial temperature of the gas, the temperature in the “zone of silence” is estimated to be about 10 K. The gas in the “zone of silence” is isentropic i.e. the amount of collisions in the “zone” are minimized due to the expansion and cooling process. The length, x , of the “zone of silence” is given by:

$$\frac{x}{d} = \frac{2}{3} \sqrt{\frac{P_0}{P_b}} \quad (51)$$

where d is the inner diameter of the needle, P_o is the driving pressure of the gas, and P_b is the background pressure in the chamber [80]. In the case of this particular experiment, the length of the “zone of silence” is approximately 20 cm. By placing a skimmer within the “zone of silence”, one can create a target gas beam of only the isentropic gas traveling at supersonic speeds. The momentum of the gas perpendicular to the direction of flow is greatly reduced by “skimming” away the hot component of the target gas leading to momentum resolutions around 0.15 atomic units [36]. The unwanted portion of the jet, the nonisentropic gas with large density, pressure, velocity, and temperature distributions, is removed by the skimmer, which reduces the amount of background collisions in the target chamber further improving the overall momentum resolution. The skimmer also keeps shockwaves from supersonic expansion out of the target chamber. In the case of this particular experiment, the skimmer was 0.8 mm inner diameter and the relative distances between the projectile beam centerline and the needle and skimmer were approximately 30mm and 20mm, respectively.

3.6 RECOIL-ION MOMENTUM SPECTROMETER

The recoil-ion momentum spectrometer is shown in Figure 3.9. The ions produced in the collision with the projectile beam are extracted by a weak electric field and detected by a two-dimensional position-sensitive detector (see Section 3.7.1). The three-dimensional momentum of the recoil ion is determined by its final position on the detector along with its time-of-flight through the spectrometer. The coordinate system used in the following analysis is as follows: the direction of the electric field of the

spectrometer is the x-axis, the direction of the supersonic target jet is the y-axis, and the initial (precollision) direction of the projectile beam is the z-axis.

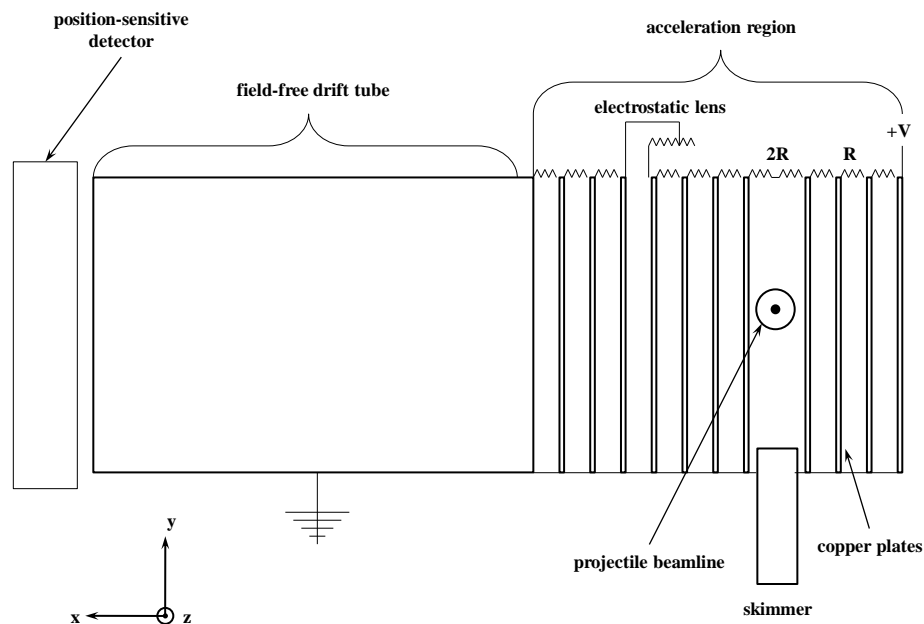


Figure 3.9. Schematic of recoil ion spectrometer.

The recoil-ion spectrometer consists of a set of copper plates with a circular opening cut out and a cylindrical drift tube. The copper plates are separated by nylon spacers and are connected in series with one another by a resistor chain. The final copper plate is connected to the drift tube, which has the same diameter as the circular opening cut in the copper plates. Both the drift tube and the final copper plate are grounded. When a positive voltage is applied to the end of the copper plates opposite of the drift tube, an electric field is created in the direction of the drift tube. Between two of the plates, there is a potentiometer allowing for variable resistance, which acts as an

electrostatic lens. Otherwise, the distance and resistance between two plates are equivalent for all plates, thus, creating two uniform electric fields on either side of the lens.

The potential difference across the acceleration region is 50 V over a length of 14 cm, which creates an average electric field of 3.6 V/cm. The total length the ions travel in the x direction is 33.3 cm, 9.5 cm in the acceleration region and 23.8 cm in the field-free region.

The momentum of the recoil ion in the direction of the electric field is determined by its time-of-flight through the acceleration region of the spectrometer:

$$p_x^{rec} = \frac{qU}{l}(t_o - t) \quad (52)$$

where q is the charge of the ion, U is the potential difference over the copper plates, l is the total length of the acceleration region, and t_o is the time-of-flight of ions with zero momentum in the x-direction. In the directions perpendicular to the electric field where there is no force acting on the ions, the recoil ion momentum is simply determined by the displacement of the ion:

$$p_y^{rec} = \frac{m}{t}\Delta y \quad (53)$$

$$p_z^{rec} = \frac{m}{t}\Delta z \quad (54)$$

where m is the mass of the ion and t is its time-of-flight through the spectrometer.

In order to perform high resolution momentum spectroscopy, it is necessary to account for the finite volume in which the collision takes place. In other words, ions with the same momentum vector, but occurring at different places in the interaction region, need to have the same time-of-flight through the spectrometer and hit the detector in the same area. In the direction of the electric field, this is accomplished by Wiley-McLaren

time-focusing [81]. The physics behind this type of time-focusing are as follows: ions created closer to the detector have a shorter path length through the spectrometer relative to ions created farther away from the detector. However, the ions created closer to the detector gain less kinetic energy from the electric field relative to ions created farther away from the detector. By allowing a “relaxation” period, or time lag, where no field is acting on the ions, namely, the drift tube, it is possible for ions created at different positions with the same initial momentum to arrive at the detector at the same time. For a single uniform electric field, a field-free region double the length of the acceleration region is needed for optimal focusing. For two uniform electric fields, the ratio of field-free region to acceleration region doesn’t have such a simple geometry; however, it is possible to calculate this geometry and is done so in Wiley et al. [81]. In the PROTRIMS experiment at Missouri S&T, the interaction length in the x-direction is about 0.15 mm, an order of magnitude smaller than in typical experiments using higher energy ion beams, due to the projectile beam-defining slits. This leads to a much smaller effect on the overall resolution in the x-direction due to the finite interaction volume. In the direction perpendicular to the electric field, the finite interaction volume is accounted for through the use of an electrostatic lens, which focuses the recoil ion momentum in the y and z directions. By placing the detector at the focal point of the lens, ions created at different y and z positions, but with same y and z momentum, will hit the detector in the same place. This type of spatial-focusing still leaves an ion’s displacement on the detector being proportional to its initial momentum [13]. To completely account for the finite interaction volume, the focal points due to spatial- and time-focusing have to occur at the recoil detector where the position and time signals for the recoil ions are measured.

3.7 EXPERIMENTAL EQUIPMENT

3.7.1 Position-Sensitive Detectors. The position-sensitive detectors (PSD) collect the relevant data from each collision, which is eventually analyzed to determine the particle's momentum and the differential cross section for that particular collision process. Since the momentum and position of particles involved in atomic collisions are far too small to be measured using conventional optical techniques, it is necessary to correlate a particle's position and momentum with a measurable electronic signal. A microchannel plate (MCP) detector, schematically shown in Figure 3.10, is used to create a large enough electronic signal to perform measurements by producing an electron cloud from a single collision event. The position and timing signal of the electron cloud is, then, measured on a wedge and strip anode (WSA), seen in Figure 3.11. A schematic of the entire position-sensitive detector is given in Figure 3.12.

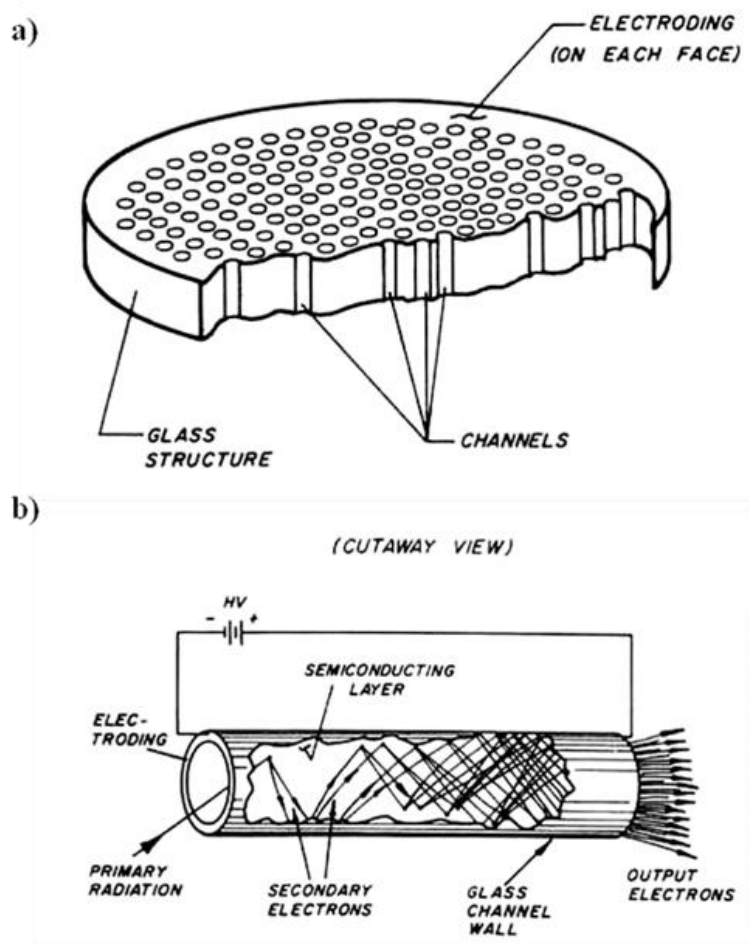


Figure 3.10. Schematic of a microchannel plate detector (a) and a single channel electron multiplier (b) with electron multiplication dynamics [82].

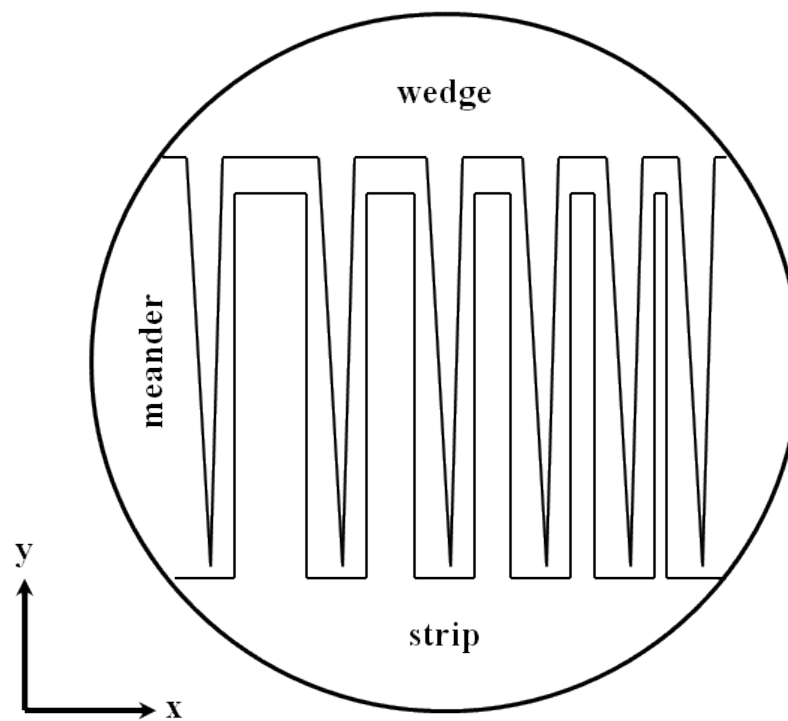


Figure 3.11. Schematic of a wedge and strip anode.

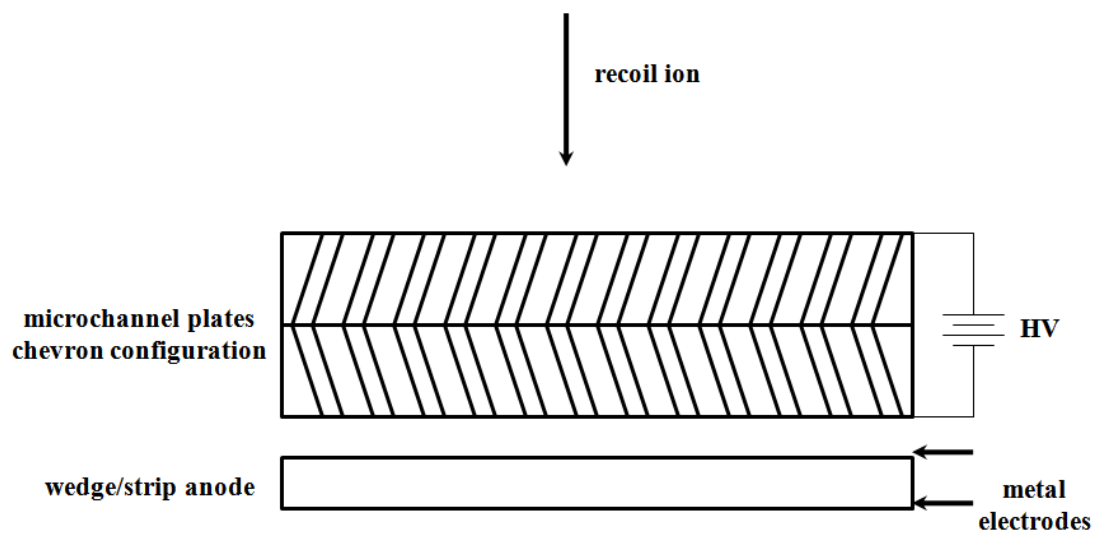


Figure 3.12. Schematic configuration of MCP and WSA used in experiment.

A microchannel plate detector consists of an array of $\sim 10^4$ - 10^7 microscopic channel electron multipliers (CEM) oriented parallel to one another. MCPs are typically made from a metal-coated glass while the CEMs are coated with a semiconductive material of high resistivity ($\sim 10^9 \Omega$) known as a continuous dynode. By placing a large negative potential difference (~ -2000 V) between the front and the back of the MCP (see Figure 3.12), one can both induce secondary electron emission and restore the electrons lost in the secondary electron emission process. The CEMs are oriented at a nonzero angle normal to the surface of the MCP in a “chevron” configuration (see Figure 3.12). This configuration restricts the amount of positive ions produced at the back of the MCP from traveling through the CEMs which would reduce the amount of secondary electrons produced [82]. The circular MCPs used in this experiment have an active detection diameter of 46 mm. The inner diameter of the individual CEMs is 10 μm with 12 μm spacing between CEMs. The lattice of CEMs are oriented at an angle of 12° normal to the surface of the MCP. The timing signal is measured from the back of the MCP and has a resolution of less than 100 ps [82].

As shown in Figure 3.10b, a single CEM works by producing an electron avalanche from a single collision with the MCP surface by the primary radiation, in this case, H^+ . The initial collision with the surface of the MCP creates a few secondary electrons. These electrons are then accelerated towards the back of the MCP and, in the process, suffer collisions with the walls of the CEM producing secondary electrons of their own. With continuing wall collisions, there is an exponential growth in the number of electrons produced ($\sim 10^7$ electrons), thereby, creating a large enough electronic signal to measure on the wedge and strip anode at the back of the MCP.

A wedge and strip anode is a ceramic plate with a layer of Germanium, a semiconductor, baked on one side and three conducting electrodes applied to the other side (see Figure 3.11). An electron cloud that hits the Ge layer gives off an image charge on the back of the WSA which is picked up on the electrodes. Of the three conducting electrodes, two of them are position-dependent: the wedge electrode has a y-dependence and the strip electrode has an x-dependence. The meander electrode picks up the remaining charge that doesn't hit either the wedge or the strip allowing the entire charge of the electron cloud to be collected. The position of the electron cloud as well as its source, the primary radiation, is given by the charge distribution across the three electrodes:

$$x = \frac{Q_s}{Q_{total}} \quad (54)$$

$$y = \frac{Q_w}{Q_{total}} \quad (56)$$

$$Q_{total} = Q_s + Q_w + Q_m \quad (57)$$

where Q_s is the charge on the strip, Q_w is the charge on the wedge, Q_m is the charge on the meander, and Q_{total} is the sum of all three electrodes. The position equations are divided by the total charge to normalize the position with respect to the total charge of the electron cloud. For example, a charge that hits in the upper left side of Figure 3.11 would have a large Q_s and Q_w while a charge that hits in the lower right side would have a relatively small Q_s and Q_w . Therefore, a WSA is able to determine the primary radiation's position with a resolution of 50 μm [83].

3.7.2 Data Acquisition Electronics. Figure 3.13 shows a block diagram of the electronics used to collect DDCS_p . Initially, the projectile detector signals had to be transformed from the high voltage plateau of the decelerator to laboratory ground. For

the timing signal coming from the back of the microchannel plate, this was done by converting the electric signal to a light signal using an optical coupler and the light signal was then detected by a photo-multiplier located at ground potential. The three signals from the wedge-and-strip anode, which contain the position information, were converted to optical analog signals, transported to ground potential through fiber optics, and then converted back to electrical signals. The fast timing signals from the back plate of the projectile and recoil-ion detectors served as start and stop signals of a time-to-amplitude converter (TAC) in a coincidence set-up (see Section 4.2). The output of the TAC, i.e. the coincidence time, is essentially the time of flight of the recoil ions plus a constant offset due to the constant (because of the fixed energy loss) time of flight of the projectiles. The three position signals along with the coincidence time signal are converted to digital signals by an analog-to-digital converter (ADC) and, finally, analyzed through data analysis software on the computer.

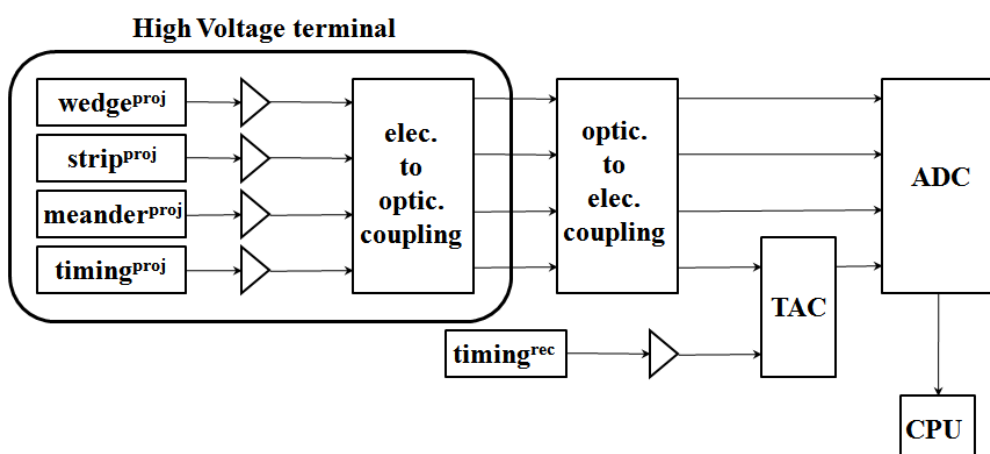


Figure 3.13. Block diagram of the data collection electronics used for DDCS_p.

4. DATA ANALYSIS

4.1 OVERVIEW

In Figure 4.1, a typical coincidence time spectrum is shown. Using simple kinematics for motion of a charged particle in a uniform electric field, it is straightforward to show that the time of flight is proportional to the square root of the mass to charge ratio of the particle (time of flight $\propto v^{-1}$ see equation (31)). Ionization of atomic hydrogen and of undissociated molecular hydrogen therefore lead to separate peak structures at about 4.3 and 6.3 μsec , respectively, in the coincidence time spectrum. From the intensity ratio between the proton and H_2^+ peaks we estimate the degree of dissociation, δ , to be about 30 to 40%. About the same value was reached in studies of charge exchange processes using a similar design for the atomic hydrogen source [50]. This relatively small δ is the price to be paid for a design that allows performing momentum-analysis of the recoil ions (see Section 3.1). Although this feature was not needed in the measurement of the DDCS_p reported here, it is necessary for experiments studying FDCS , which are currently in progress. In order to convert raw data from the computer to normalized DDCS_p , one must: 1) “clean-up” the projectile position spectrum by removing events that didn’t occur from ionization events in a $p + \text{H}$ collision. Such unwanted events can result from processes other than ionization, which leave the projectiles positively charged (e.g. excitation or elastic scattering), as well as from ionization of undissociated H_2 or of the residual gas in the beamline. 2.) “Clean-up” the projectile position spectrum by removing events in which the detected projectile and the detected recoil-ion originated from two different collisions. 3) Calibrate the scattering

angle from the position spectrum, and 4) normalize the DDCS to an absolute scale using measured single differential cross sections of H and H₂ (when H-data are not available, see below) for a system of the same parameters. In the next section, the selection of true p + H ionization events is described.

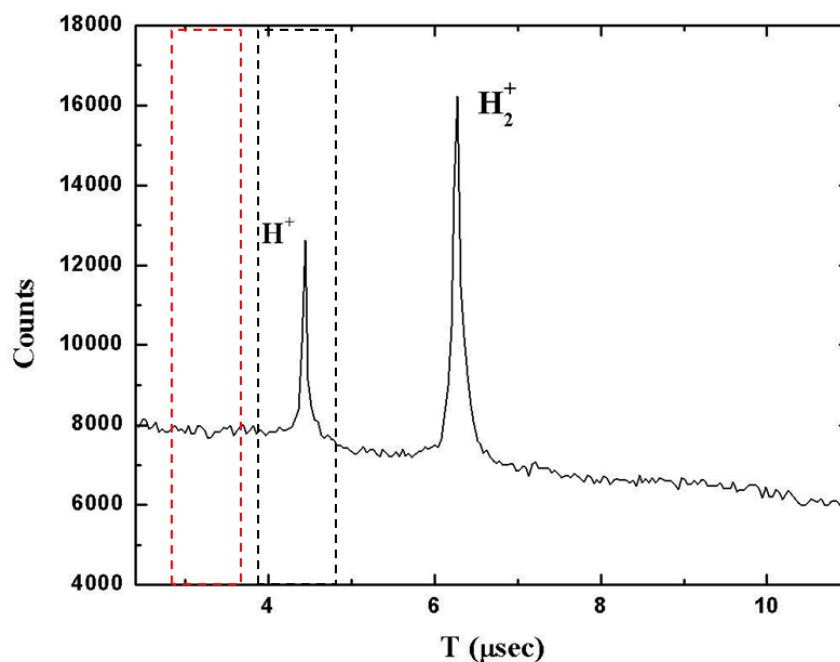


Figure 4.1. Coincidence time spectrum with initial time window (black) and random window (red).

4.2 COINCIDENCE TIME SPECTRUM

For each ΔE , a projectile position spectrum was generated with a condition on the proton coincidence time peak (black window in Figure 4.1). A typical x-component of the projectile spectrum is shown in Figure 4.2 with a condition on the proton coincidence time peak. The contributions to the coincident position spectrum from unwanted events

(see Section 4.1) underneath the time peak were subtracted as follows: first, the total number of counts in the random spectrum underneath the proton time peak was determined from a spline fit. Only the regions of the time spectrum outside the peak structures were used to determine the fitting parameters, but the fitting curve was calculated for the entire spectrum. Then, a second window was set to the left of this peak with a width which was adjusted so that the number of counts in this window was equal to the number of counts underneath the peak obtained from the spline fit. A second projectile position spectrum was generated for this window and subtracted from the spectrum with the condition on the time peak. A typical x-component of the projectile spectrum after this subtraction is shown in Figure 4.3. Since the x-component of the projectile position corresponds to the scattering angle and these spectra were recorded for fixed ΔE , they are directly proportional to the $DDCS_p$.

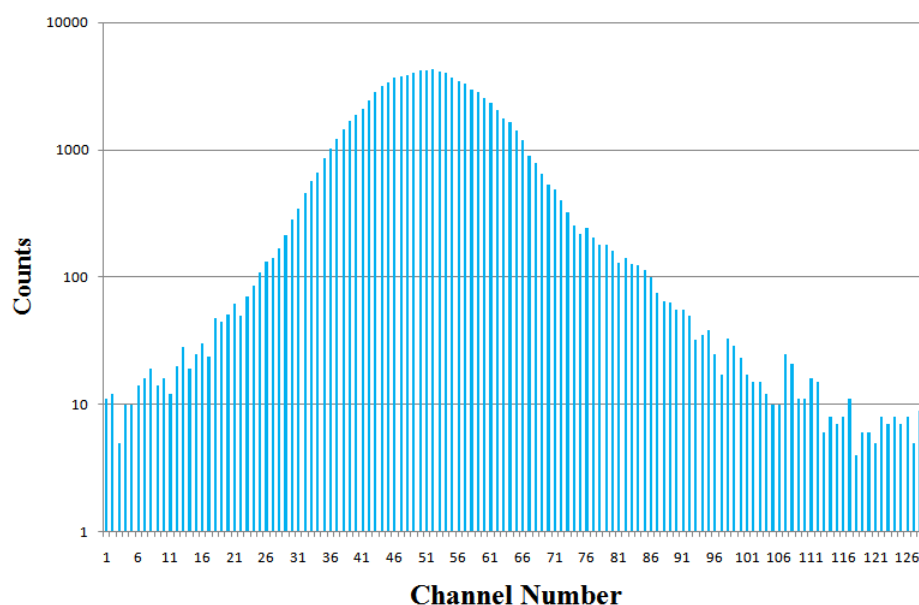


Figure 4.2. The x-component of the projectile position spectrum with a condition on the time peak for H^+ before random coincidence subtraction.

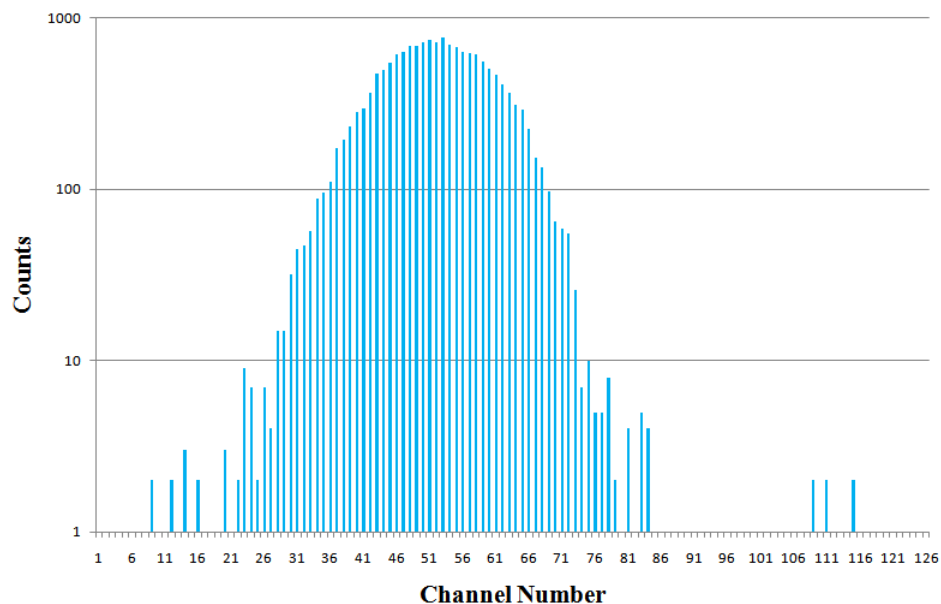


Figure 4.3. The x-component of the projectile position spectrum with a condition on the time peak for H^+ after random coincidence subtraction.

4.3 SCATTERING ANGLE CALIBRATION

The scattering angle calibration of the position spectrum was performed using two independent methods. First, a position spectrum was recorded for a fixed ΔE for 75 keV $p + He$ collisions. The calibration factor was adjusted so that the scattering angle dependence of the $DDCS_p$ measured earlier for this collision system without using a position-sensitive detector [51], was reproduced. In the second method, the channel number of the x-position was first calibrated into millimeters using the known size of the active area of the anode. Next, the distance from the collision region to the decelerator, the length of the decelerator column (where the beam diverges due to the deceleration), and the distance from the end of the column to the entrance of the analyzer were measured accurately and the length of the path through the analyzer was calculated from

its geometric properties and the applied voltage. Using these data and accounting for the divergence in the decelerator column, it is straight-forward to convert the x-position to scattering angle [84]. The calibration factor obtained from these two methods agreed with each other within 3%. The position resolution of 100 μm FWHM resulted in an overall angular resolution (including the divergence of the incident beam) of better than 0.1 mrad FWHM.

4.4 NORMALIZATION

To obtain the DDCS_p on an absolute scale the double differential position spectra integrated over the projectile solid angle were normalized to single differential cross sections (SDCS) as a function of ΔE measured by Park et al. [49]. To normalize a $\text{DDCS}_p(\theta_p, \Delta E)$ to $\text{SDCS}(\Delta E)$, one must integrate DDCS_p over all projectile scattering angles. In an experiment, one normally begins with a doubly differential rate, $\frac{d^2 N}{d\Omega_p d\Delta E}$ which is related to the DDCS_p by:

$$\frac{d^2 \sigma}{d\Omega_p d\Delta E} = C \frac{d^2 N}{d\Omega_p d\Delta E} \quad (58)$$

where C is a constant of proportionality. The SDCS is then related to the doubly differential rate by:

$$\text{SDCS}(\Delta E) = 2\pi C \int \frac{d^2 N}{d\Omega_p d\Delta E} \sin \theta_p d\theta_p, \quad (59)$$

which then normalizes the DDCS_p on an absolute scale. When the SDCS of Park et al. were integrated over ΔE , they were too large by a factor of 1.8 compared to recommended total cross sections based on a large collection of experimental data [85]. Therefore, the DDCS_p normalized to the SDCS of Park et al. were further divided by 1.8.

On the other hand, one should not rule out the possibility that the magnitude of the integrated SDCS by Park et al. are actually more accurate than the recommended total cross sections and this should be kept in mind when comparing to theory. Furthermore, no measured SDCS are available for $\Delta E > 45$ eV. Up to that energy, the data of Park et al. divided by 1.8 are exactly a factor of 2 smaller than the corresponding cross sections for H_2 . At $\Delta E = 50$ and 53 eV, we thus normalized our $DDCS_p$ to half the SDCS for H_2 [86]. This procedure leads to some additional uncertainties in the absolute magnitude of the $DDCS_p$ for these ΔE , especially for 53 eV, which nearly corresponds to $v_e = v_p$. At this matching velocity a step in the SDCS for $p + He$ collisions was observed [51,52], which is a manifestation of a strong second-order projectile-electron interaction. For H_2 , $v_e = v_p$ corresponds to a slightly larger ΔE than for H because of the larger ionization potential (= 15.4 eV; ionization potential of H = 13.6 eV). Therefore, in the SDCS for H_2 a step would be expected only at an ΔE larger than 53 eV, while for H 53 eV is very close to the step. This could lead to a slight overestimation of the normalized $DDCS_p$ at 53 eV, which should also be kept in mind when comparing to theory.

5. RESULTS AND DISCUSSION

5.1 OVERVIEW

From the angular calibration, cross section normalization, and coincidence measurement, one obtains absolute DDCS_p as a function of the projectile scattering angle for a specific energy loss. Formally, the doubly differential cross sections measured in this dissertation are written as: $\frac{d^2\sigma}{d\Omega_p d\Delta E}(\theta_p, \Delta E)$. To analyze the DDCS_p , the experimental data are compared to numerous theoretical models. These models include the CDW-EIS model, the 3C model, and the SBA-2C model. Several variations of each model are described in this section for the purpose of better understanding the influence of higher order contributions from the various two-particle interactions such as the PT interaction and the projectile-electron interaction. The work presented in this section follows the work of LaForge et al. [71] and Schulz et al. [87].

5.2 EXPERIMENTAL DDCS_p

In Figure 5.1, the DDCS_p are plotted for $\Delta E = 30, 40, 50,$ and 53 eV as a function of the projectile scattering angle, θ_p . The data fall off rapidly with increasing θ_p , which is a typical scattering angle dependence of cross sections for most processes. It is well known that for deflection of a proton from a free electron there is a maximum scattering angle of about 0.55 mrad [88]. Larger scattering angles in ionization of atoms must therefore be either due to the bond of the electron in the initial target ground state or due to additional deflection of the projectile from the target nucleus. Since regardless of

scattering angle any electronic transition from the ground state always requires an interaction between the projectile and the electron, ionization is expected to be dominated by three-body dynamics at large θ_p . At $\theta_p < 0.55$ mrad, on the other hand, ionization due to a binary projectile-electron interaction is kinematically possible. At small scattering angles the role of three-body dynamics is thus not immediately clear. However, the fact that we do not observe a noticeable change of slope in the angular dependence of the data around 0.55 mrad suggests that such three-body interactions are generally not negligible.

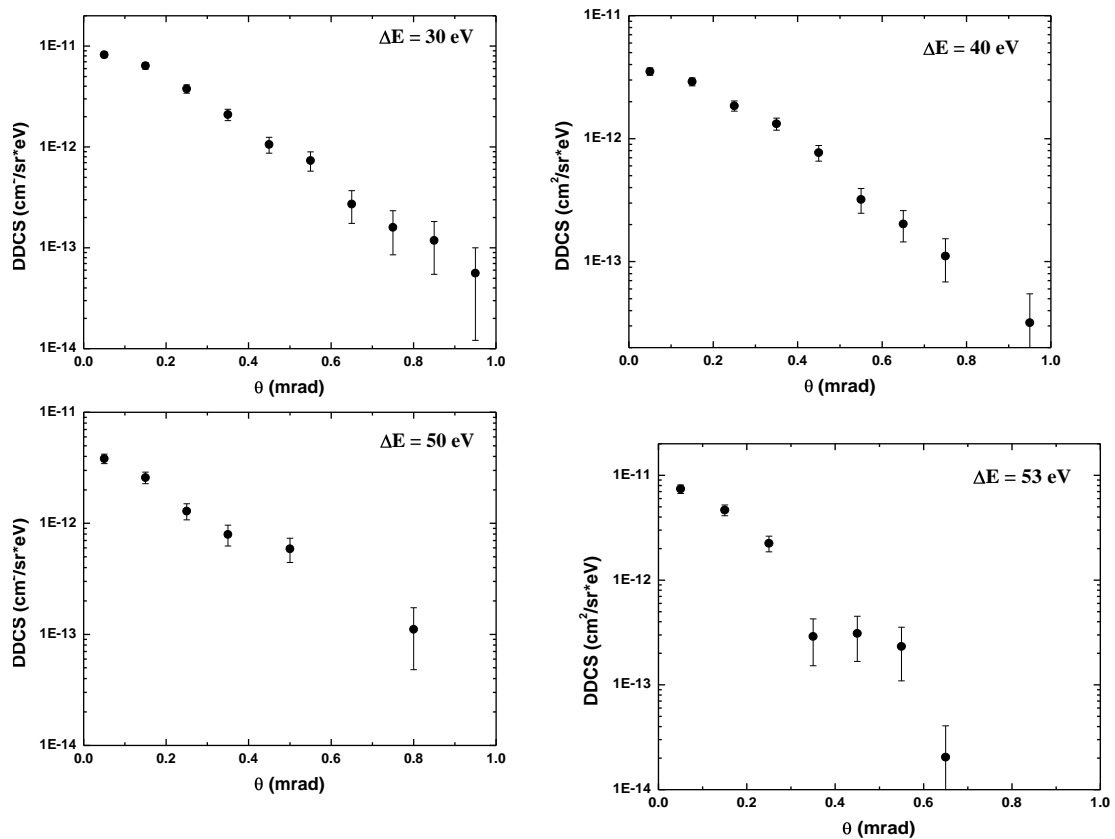


Figure 5.1. $DDCS_p$ as a function of θ_p for fixed energy losses ($= 30, 40, 50, 53$ eV). The experimental data are shown as solid circles.

The rate at which the $DDCS_p$ are dropping is not very sensitive to ΔE up to about 50 eV, however, at 53 eV the width of the $DDCS_p$ suddenly decreases significantly. The same behavior was also observed for ionization of molecular hydrogen [87] and, to a lesser extent, of helium [51,52] by proton impact at the same collision energy. It is illustrated in more detail in Figure 5.2 where the average scattering angle,

$$\theta_{avg} = \frac{\int \theta_p DDCS_p(\theta_p, \Delta E) d\Omega_p}{SDCS(\Delta E)}, \quad (60)$$

is plotted as a function of the electron to projectile speed ratio v_e/v_p for atomic (solid circles) and molecular hydrogen (open circles). For atomic hydrogen the drop in the width near $v_e/v_p = 1$ is quite obvious, but we have no data for $v_e/v_p > 1$ to determine the trend above this matching velocity. On the other hand, for the molecular hydrogen target, a pronounced minimum is observed near $v_e/v_p = 1$. This behavior can be understood in terms of a post-collision interaction (PCI) between the outgoing scattered projectile and the electron ejected by a preceding primary interaction with the projectile. Since PCI is known to maximize for $v_e/v_p = 1$ [51,52] it is plausible to interpret the sudden narrowing of the $DDCS_p$ at 53 eV as a mutual focusing effect between the outgoing projectiles and the ejected electrons due to the attractive PCI. The magnitude of this narrowing is surprising because it is much more pronounced than for a helium target, where only a change of slope, rather than a minimum, in the width of the $DDCS_p$ was observed near $v_e/v_p = 1$ [51,52].

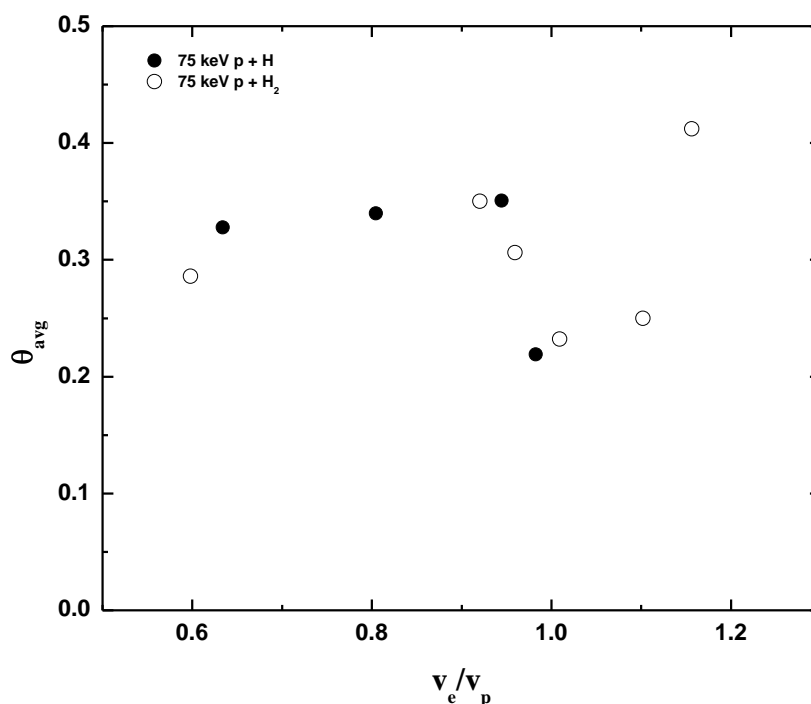


Figure 5.2. Average scattering angle as a function of the electron's speed. Open circles, molecular hydrogen target [89]; solid circles, atomic hydrogen target.

5.3 THEORETICAL DDCS_p

The data of Figure 5.1. are shown again in Figure 5.3 along with theoretical calculations. The dotted curves in Figure 5.3 show CDW-EIS calculations, which account for the PT interaction semi-classically in terms of the eikonal approximation assuming a classical trajectory of the projectile [26]. PCI is treated in terms of a distortion of the ejected electron wave by the projectile in the final state and in terms of an eikonal phase factor in the initial state. The dashed curves are also based on the CDW-EIS model, however, here, the PT interaction is accounted for by convoluting the cross sections calculated without the PT interaction with classical elastic scattering

between the heavy particles using a Monte Carlo simulation [36,37]. This model will be referred to as CDW-EIS-CL to distinguish it from the one which treats the PT interaction within the eikonal approximation (semi-classically), which will be called CDW-EIS-SC.

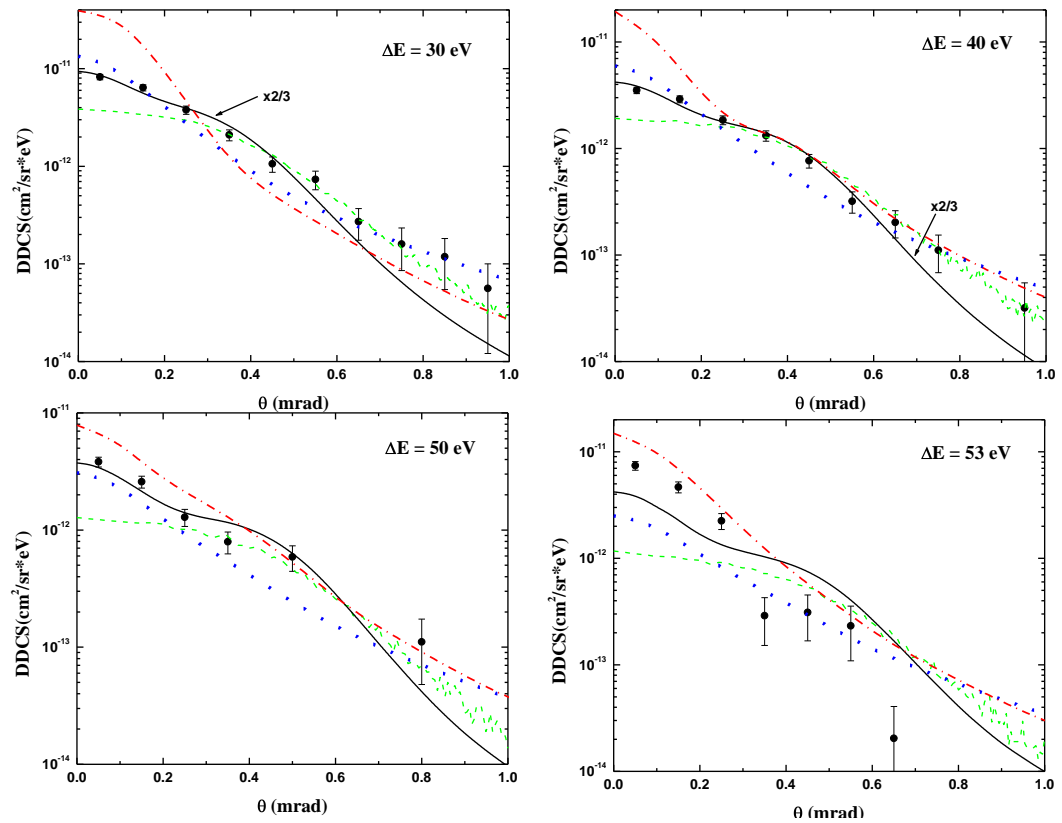


Figure 5.3 Same as Figure 5.1, but calculations are: **dotted blue curves**, CDW-EIS-SC; **dashed green curves**, CDW-EIS-CL; **dash-dotted red curves**, 3C; **solid curves**, SBA-2C.

The dash-dotted curves represent calculations based on the three Coulomb wave (3C) approach [72-74,90]. Here, the initial state is described the same way as in the FBA (i.e. a product of an eigenstate of the unperturbed target Hamiltonian and a plane wave

for the projectile). The final state is a product of three Coulomb waves describing the three two-particle subsystems (electron-target nucleus, electron-projectile, and projectile-target nucleus) so that both the PT interaction and PCI are treated in the final state. The CDW-EIS and 3C calculations are conceptually similar in that in both higher-order effects are accounted for in the final state, rather than in the operator of the transition amplitude. The CDW-EIS approach has the advantage that higher-order contributions are included in both the initial and final state while the 3C model has an edge in treating the projectile fully quantum-mechanically.

The solid curves show calculations based on a refinement of the second Born approximation [75]. However, in the final-state, the projectile is not just described by a plane wave, but, like in the 3C model, by a Coulomb wave distorted in the field of the ejected electron. Therefore, PCI is accounted for in the same manner as in the 3C calculations. In contrast, the PT interaction is treated in the operator of the second-order term of the transition amplitude rather than in the final-state wavefunction. The electronic part of the intermediate state in the Green's function is identical to the initial state so that PCI is not accounted for in the operator of the second-order term. Since the electron – target nucleus sub-system in the final state is described by a second Coulomb wave this will be referred to as Second Born Approximation – 2 Coulomb waves (SBA-2C).

5.4 THEORETICAL ANALYSIS

A comparison between the CDW-EIS-SC and CDW-EIS-CL models and the experimental data for $\Delta E = 30$ to 50 eV was initially presented by LaForge et al.[71].

Both approaches significantly improve the agreement with the data at large θ_p relative to a CDW-EIS calculation, which does not treat the PT interaction at all (CDW-EIS-noPT, not shown in Figure 5.3). At small θ_p , the CDW-EIS-CL and CDW-EIS-noPT results do not differ much. The CDW-EIS-SC calculations, on the other hand, removes the underestimation of the DDCS_p by the CDW-EIS-noPT model at $\theta_p < 0.2$ mrad. However, it leads to significant discrepancies with the data at intermediate θ_p (≈ 0.2 to 0.6 mrad), where the data are well described by the CDW-EIS-CL and CDW-EIS-noPT calculations. In the latter two, a convex curvature in the theoretical curves is found in this angular range, in accordance with experiment, which is due to binary interactions between the projectile and the ejected electron in which the recoiling target nucleus remains essentially at rest [71]. In contrast, the CDW-EIS-SC model leads to a concave curvature indicating a strong deviation from two-body kinematics due to the PT interaction. Surprisingly, the simple convolution of CDW-EIS with classical elastic scattering overall leads to a better overall agreement with experiment than treating the PT interaction semi-classically. On the other hand, for $\Delta E = 53$ eV, corresponding to $v_e = v_p$, none of the CDW-EIS calculations is in satisfactory agreement with the data and they even fail to reproduce the narrowing of the θ_p -dependence of the measured DDCS_p .

The comparison of the CDW-EIS calculations to the data especially at $\Delta E = 53$ eV shows that, apart from the PT interaction, PCI also still represents a major challenge to this model. The description of PCI in the 3C and CDW-EIS approaches are very similar and one may therefore not necessarily expect improved agreement with the data for the former model. On the other hand, the fully quantum-mechanical treatment of the PT interaction raises some hope that features due to that interaction are better reproduced by

the 3C model. Looking at the data for $\Delta E = 30$ eV, this hope appears to have been thwarted. The discrepancies to experiment are larger than for the CDW-EIS-SC results, essentially in the entire angular range. However, upon review of the other three energy losses, one sees that the 3C calculations yield significantly better agreement, at least for $\theta_p > 0.2$ mrad. It is particularly interesting (and not quite understood) that the concave curvature of the 3C-curve at $\Delta E = 30$ eV, seen in the CDW-EIS-SC calculations at all ΔE , turns into a convex curvature at 40 and 50 eV resulting in significantly improved agreement with the experimental data. Perhaps the most remarkable aspect of the 3C results is that they reproduce (apart from possibly slightly overestimating the overall magnitude) the measured DDCS_p for $\Delta E = 53$ eV fairly well, which is in sharp contrast to the CDW-EIS models. In particular, the sudden narrowing of the angular distribution of the DDCS_p relative to $\Delta E = 50$ eV is well reproduced. The 3C model thus reinforces the surprising observation that PCI is much more important in $p + \text{H}$ than it is in $p + \text{He}$ collisions [51,52].

Except for $\Delta E = 53$ eV, the SBA-2C model reproduces the shape of the θ_p -dependence of the measured DDCS_p almost perfectly. At $\Delta E = 30$ and 40 eV, there seems to be a discrepancy of about 50% in the magnitude which, however, is not necessarily significant keeping in mind the uncertainties in the normalization of the data mentioned in Section 4.4. Of all calculations presented in this section, the SBA-2C approach yields the best overall agreement with the experimental data for $\Delta E = 30$ to 50 eV. At $\Delta E = 53$ eV, it still fares clearly better than both CDW-EIS calculations, but it does not describe the magnitude and the width of the angular distribution of the DDCS_p as well as the 3C model.

5.5 THEORETICAL DISCUSSION

The comparison between experiment and theory raises several questions, the answers to which could prove important in advancing our understanding of the few-body fragmentation dynamics in simple atomic systems: 1.) Why does the classical treatment of the PT interaction within the CDW-EIS approach yield better results than the semi-classical treatment? Since we are obviously dealing with a quantum-mechanical system this should not be viewed as a success of the CDW-EIS-CL model, but rather as a significant problem with the CDW-EIS-SC model. 2.) All calculations presented so far conceptually contain essentially the same physics and only the technical treatment of the Physics is different. Why, then, do they differ so much (up to an order of magnitude in some regions) from each other in the numerical results? 3.) Why do the CDW-EIS and SBA-2C calculations not reproduce the strong focusing effect due to PCI at $\Delta E = 53$ eV seen in the experimental data, and why is the 3C calculation much more successful in this regard, although it seems conceptually very similar to CDW-EIS in its treatment of PCI? In the following section, these questions are addressed by analyzing in more detail to what extent the various higher-order contributions are described in the different models.

To start the discussion of higher-order contributions, it is worth pointing out that any interaction included in the final-state wavefunction is conceptually treated to all orders of perturbation theory. However, since in practice it is not possible to find an exact wavefunction, not all, or perhaps none of the higher-order contributions are treated completely and/or accurately. On the other hand, any interaction that is only included in the operator is treated to whatever order the Born series is expanded. The advantage of treating the interaction in the operator is that, in principle, each order can be treated

accurately, unless additional approximations (like e.g. the Closure Approximation) are employed. An important question then is: what is more important, to include the various interactions to as many orders as possible or to treat specific higher-order contributions (especially the second-order terms) as accurately as possible? The answer to this question may well be different for different interactions.

The 3C wavefunction is known to only be accurate if at least one particle is far away from the other two particles [91]. Furthermore, if the PT interaction leads to a significant deflection of the projectile, one would expect that, on average, all three particles have to approach each other to relatively small distances, at least at large θ_p , because the ejection of the electron requires a relatively close encounter with the projectile. This would suggest that treating the PT interaction in terms of a Coulomb wave may result in some inaccuracies (see also [26,27]). Conversely, if the perturbation η (projectile charge to speed ratio) of the collision is not too large, the magnitude of the various expansion terms usually decreases rapidly with increasing order. Treating the PT interaction within the SBA may therefore be a viable approach.

The framework for higher-order contributions in the projectile-electron interaction, i.e. for PCI, is quite different. Because this interaction is attractive it tends to significantly reduce the average separation between both particles and to increase the time they stay close together. At the same time, the projectile-electron subsystem rapidly departs to a large distance from the target nucleus at nearly the projectile speed, which is much larger than the relative speed between the projectile and the electron. Therefore, the condition for the validity of the 3C wavefunction is satisfied for most of the time, especially at $\Delta E = 53$ eV (corresponding to a minimized average relative speed ($|\mathbf{v}_e - \mathbf{v}_p|$))

≈ 0). On the other hand, because of the long interaction time between the projectile and the electron one cannot assume that terms beyond second-order are insignificant. These arguments suggest that it is more appropriate to describe higher-order effects in the projectile-electron interaction, in contrast to the PT interaction, in terms of a final-state Coulomb wave.

In order to test the above hypotheses, the various theoretical models are analyzed in more detail by: starting with the FBA (which only includes first order processes), and successively adding the PT interaction and PCI using the respective method of these models with goal of seeing each interactions relative importance in the $DDCS_p$. The experimental data of Figure 5.1 are shown again in Figure 5.4, but this time they are compared to different theoretical curves. The dotted lines represent the FBA results. The dashed lines show calculations in which the second order term of the SBA-2C model was omitted. In other words, the final state in the FBA was replaced by a product of two Coulomb waves representing the electron-projectile and electron-target nucleus subsystems. Formally, this is a 3C calculation. However, for the PT interaction in the 3C wavefunction, further approximations were made (peaking approximation), which almost completely remove effects due to that interaction on the cross sections. This 2C model thus accounts for PCI, but only to a very limited extent for the PT interaction. Furthermore, replacing the 2C wavefunction in the SBA-2C model by a product of a Coulomb wave for the electron-target nucleus subsystem and a plane wave for the projectile (which is the final state wavefunction in the Born approximation) results in the dash-dotted curves. This calculation, which we call SBA, contains the PT interaction, but not PCI. Finally, the solid curves show the SBA-2C results.

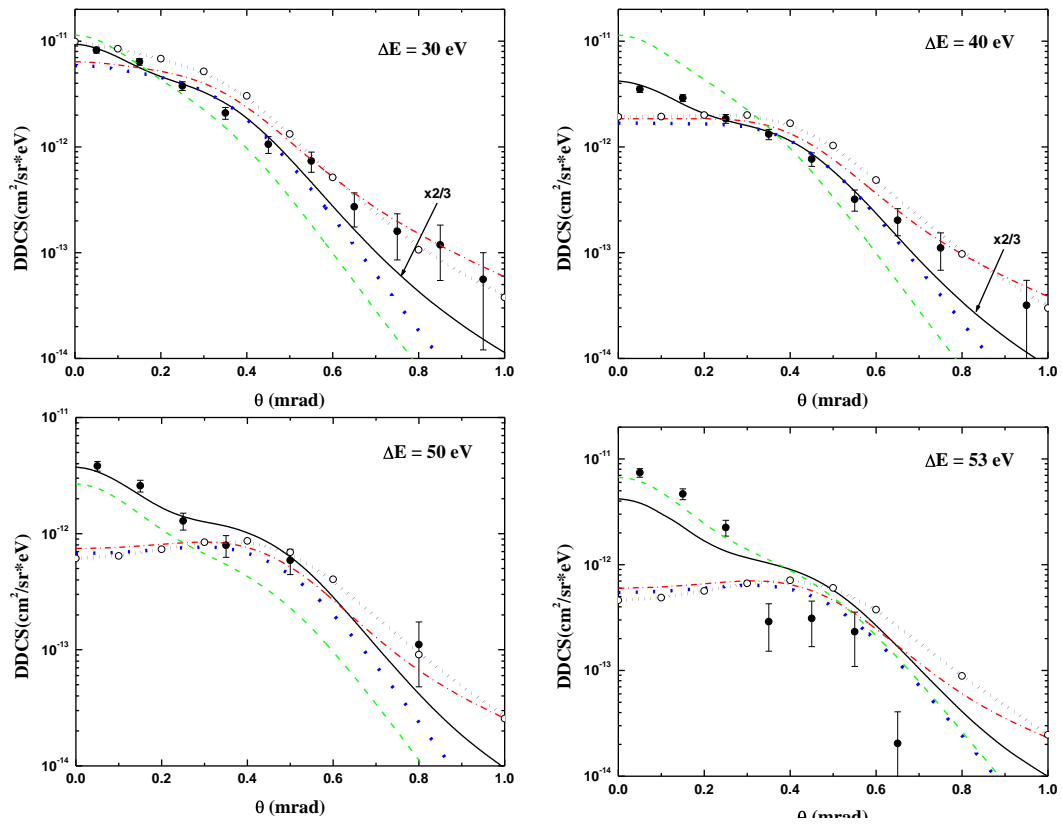


Figure 5.4. Same as Figure 5.1, but calculations are: **dotted curves**, FBA; **dashed curves**, 2C; **dash-dotted curves**, SBA; dot-circled curves, EA; solid curves, SBA-2C.

First, the lowest energy, $\Delta E = 30$ eV, is considered, which corresponds to the largest $|\mathbf{v}_e - \mathbf{v}_p|$ of the four energy losses studied here, i.e. the influence of PCI should be minimized. Therefore, $\Delta E = 30$ eV should give the best analysis of the effects of the PT interaction. Indeed, with decreasing ΔE , the difference between the 2C and FBA results systematically decrease. One might therefore suspect that an approach only accounting for the PT interaction, but not for PCI, already provides an adequate description of the ionization process. Indeed, with decreasing ΔE , the SBA results systematically approach both the SBA-2C calculation and the experimental data and are in reasonable agreement

with the latter at $\Delta E = 30$ eV. On the other hand, results obtained from the eikonal approximation [93] (EA, dot-circle curves in Figure 5.4), which roughly corresponds to removing PCI from the CDW-EIS-SC calculations, compare still reasonably well, but less favorable to the measured data than the SBA. This confirms that the PT interaction is more appropriately treated in the operator of the second-order amplitude than in the final-state wavefunction. It is interesting to note that the CDW-EIS-CL (see Figure 5.3) calculation look quite similar to the SBA. Apparently, the convolution of CDW-EIS-noPT with classical elastic scattering represents a reasonable simulation (apart from the PCI contributions not included in the SBA) of the SBA, which explains why CDW-EIS-CL yields better results than CDW-EIS-SC.

Next, the influence of PCI on the DDCCS_p in the various models is considered. For $\Delta E = 53$ eV, one might expect the PT interaction to play only a minor role compared to PCI because $|\mathbf{v}_e - \mathbf{v}_p|$ is very small. However, this assumption should be applied cautiously because it cannot be ruled out that the focusing effect due to PCI is at least partly based on an interplay with the PT interaction. To illustrate this point, it is helpful to view the ionization process classically in terms of a sequence of collisions between the various particles in the system as shown in Figure 5.5. The process starts with the primary interaction between the projectile and the electron lifting it to the continuum (ionization). As a result of this collision, the two particles now go apart. Classically, any further interaction between the projectile and the electron must be preceded by a redirection of either the projectile or the electron through a collision with the target nucleus. Therefore, the focusing effect may be due to: a) a projectile-electron – electron-target nucleus – projectile-electron (PE-ET-PE) or b) a projectile-electron – projectile-

target nucleus – projectile-electron collision (PE-PT-PE) sequence. The PE-ET-PE sequence is included in the CDW-EIS-noPT and 2C calculations, but the sequence PE-PT-PE is only accounted for by the models treating all interactions (CDW-EIS-SC, 3C, and SBA-2C).

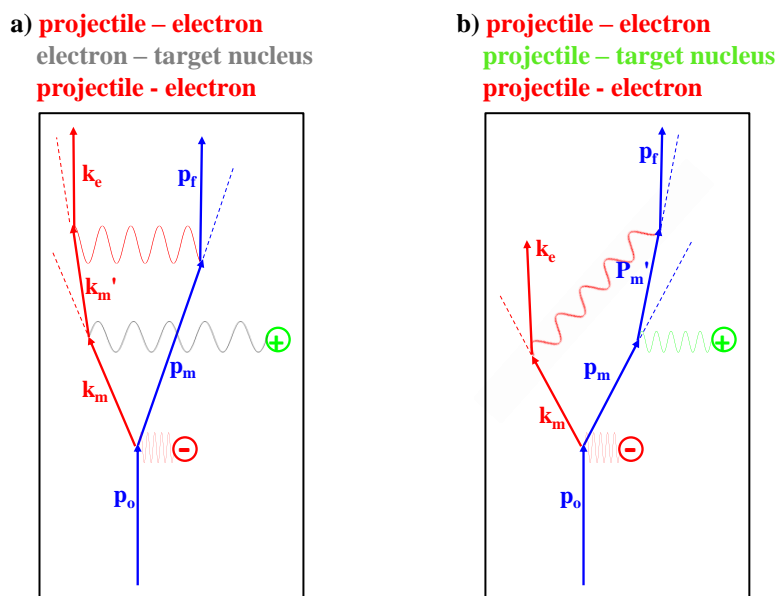


Figure 5.5. Vector diagrams of two classical sequences of interactions leading to PCI involving an interaction between the target nucleus and either the electron (a) or the projectile (b).

To evaluate the contributions of the two sequences described above, a comparison is made between the experimental data and: the SBA-2C, 2C, and FBA calculations in Figure 5.4; the CDW-EIS-SC (solid curves), CDW-EIS-noPT (dashed curves), and FBA calculations (dotted curves) in Figure 5.6; and the 3C (solid curves), 2C (dashed curves) and FBA calculations (dotted curves) in Figure 5.7.

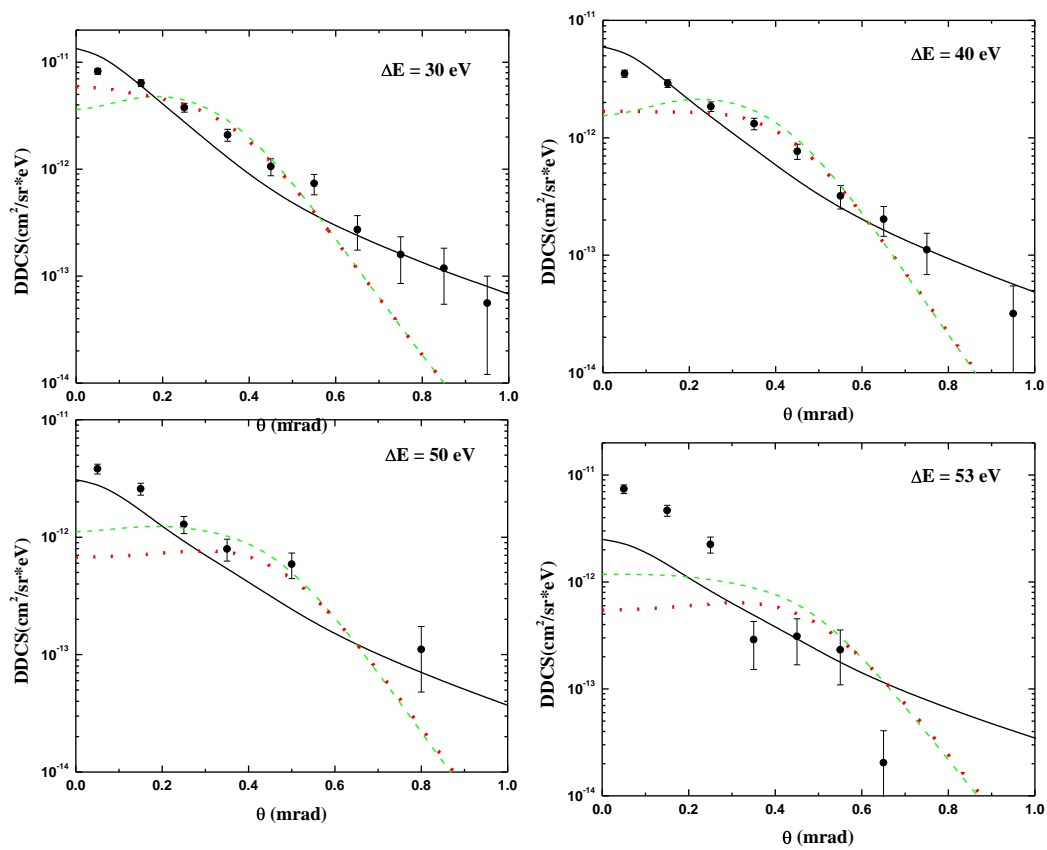


Figure 5.6. Same as Figure 5.1, but calculations are: **dotted curves**, FBA; **dashed curves**, CDW-EIS-noPT; **solid curves**, CDW-EIS-SC.

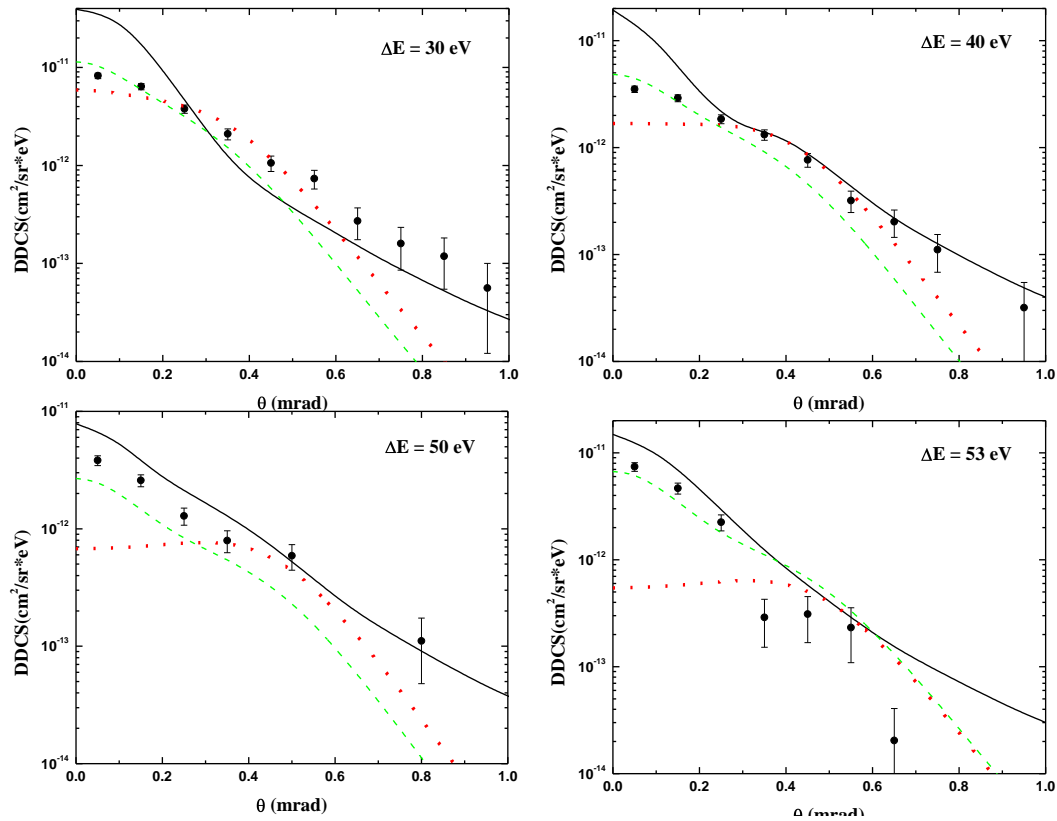


Figure 5.7. Same as Figure 5.1, but calculations are: **dotted curves**, FBA; **dashed curves**, 2C; **solid curves**, 3C.

In the CDW-EIS approach (see Figure 5.6), the PE-ET-PE sequence seems to hardly contribute at all to the focusing. Although at $\Delta E = 50$ and 53 eV the intensity at small θ_p is enhanced in the CDW-EIS-noPT calculation compared to the FBA, the width of the angular distribution is not increased much. Only after the PT interaction is included (CDW-EIS-SC), a pronounced narrowing compared to the FBA is observed. At $\Delta E = 30$ and 40 eV, the intensity at small θ_p even drops below the FBA results if the PT interaction is not accounted for. One then concludes that in the CDW-EIS approach the

focusing due to PCI is predominantly produced by the PE-PT-PE sequence (see Figure 5.5b).

A very different picture emerges from an analysis of the SBA-2C model (Figure 5.4). The 2C calculation (obtained when the PT interaction is removed from the SBA-2C model) leads to a strong narrowing of the angular distribution of the DDCS_p compared to the FBA, which becomes increasingly pronounced approaching $\Delta E = 53$ eV. In the SBA-2C results, no further narrowing relative to the 2C calculations is observed; on the contrary, a considerable broadening is found instead. Therefore, in the SBA-2C model the focusing due to PCI is clearly dominated by the PE-ET-PT sequence (see Figure 5.5a), in sharp contrast to the CDW-EIS results.

Finally, the relative importance of the PE-ET-PE and PE-PT-PE sequences in the 3C model seems to be somewhere between the CDW-EIS and SBA-2C models. In addition to the substantial narrowing in the 2C results relative to the FBA, discussed above, the width in the 3C calculations is considerably reduced compared to the 2C results. The relative contributions of both sequences in the 3C model depends on ΔE : at 30 eV the sequence involving the PT interaction seems to be slightly more important while at 53 eV most of the focusing appears to come from the sequence involving the electron-target nucleus interaction.

Since the SBA-2C model yields the best overall agreement with the experimental data, one then concludes that the focusing due to PCI is predominantly caused by the PE-ET-PE collision sequence. Only at $\Delta E = 53$ eV is the 3C calculation in better agreement with the data than the SBA-2C results, but at this ΔE the former also predicts a dominance of the PE-ET-PE sequence. In fact, here the 2C calculation reproduces the

data better than the 3C and SBA-2C models suggesting that both overestimate the importance of the PT interaction at 53 eV.

Based on the analysis of the three different models presented here, the hypothesis that the PT interaction is more appropriately treated within the SBA, but that for describing PCI the 3C approach is more suitable, is confirmed. Now, it is possible to provide partial answers to some of the questions raised above. 1) The classical treatment of the PT interaction within the CDW-EIS model works better than the semi-classical approach because the convolution with elastic classical scattering represents a good simulation of the SBA (although it is unclear why this is the case). 2) The three theoretical models yield very different results because the description of the underlying ionization dynamics is quite sensitive to the technical method of treating each interaction. For example, in all three models the PT interaction is crucially important, but only in the CDW-EIS approach does it play an overwhelming role in the focusing due to PCI. 3) The question why the 3C model is more successful than the other models in describing the narrowing of the angular distribution of the $DDCS_p$ at $\Delta E = 53$ eV remains to a large extent unanswered. It seems plausible that the severely underestimated contribution of the PE-ET-PE sequence to the focusing is closely related to the lack of success of the CDW-EIS approach in that regard. But, it is not clear why these contributions are so much weaker than in the 3C model since the treatment of the projectile-electron interaction is very similar in both models.

6. CONCLUSIONS AND OUTLOOK

6.1 CONCLUSIONS

In this dissertation, a thorough analysis was given of doubly differential ionization cross sections for fixed projectile energies as a function of scattering angle for 75 keV p + H collisions. The data was compared to three different models, all treating higher order interactions of perturbation theory. Nevertheless, major differences between the various calculations were found. The SBA-2C model is overall in good, but not perfect, agreement with the measured data and the 3C model reproduces the measured cross sections for $\Delta E = 53$ eV reasonably well.

The magnitude of the differences among the calculations, and to some extent also to the experimental data, is surprising since p + H represents the simplest system for which ionization can occur and theory is not plagued by having to deal with a complicated many-electron state. Especially the discrepancies between the CDW-EIS-SC model and the measured cross sections is disconcerting since the same model yielded excellent agreement with experiment for the more complex collision system p + He at the same collision energy [18]. On the other hand, these large differences between the various models show that the cross sections are quite sensitive to the details of the description of the ionization dynamics. The experimental data can, therefore, be used to check the validity of the approximations used in theory and to determine the most appropriate approaches to account for the higher-order contributions from the various interactions in the collision system.

The comparison between experiment and theory suggests that the projectile-target nucleus interaction is best accounted for in the operator of a second-order term of the transition amplitude. Terms beyond second order in this interaction do not appear to be very significant, at least for this collision system. For the projectile-electron interaction, in contrast, higher-order contributions are probably not negligible (due to the overall increased interaction time) and it is, therefore, more feasible to treat this interaction in the final state wavefunction. The SBA-2C model combines the favored methods of including both interactions and as a result yields the best overall agreement with experiment among the models presented here. Furthermore, the analysis in Section 5.5 reveals that a sequence of interactions between the electron and the two nuclei leads to a strong narrowing of the angular distribution of the DDCS_p . In contrast, the PT interaction, which generally plays an important role in the ionization dynamics especially at large scattering angles, hardly contributes to this focusing effect.

6.2 OUTLOOK

The success of the SBA-2C model could potentially also be of considerable relevance with respect to the unexpected features observed in the FDSC for electron emission into the perpendicular plane mentioned in the introduction (Section 1). Although these observations were interpreted in terms of the PT interaction, calculations which account for it in the wavefunction, such as the distorted wave models, were not able to reproduce the experimental data [2]. However, at this point, calculations of FDSC for the perpendicular plane based on the SBA-2C (or similar) model have not yet been reported. The significant differences between the calculations presented here along with

the success of the SBA-2C model demonstrated in this dissertation raises hope that it may be able to reproduce these FDCS data as well and thus solve a long-standing puzzle.

Although from the present data a good understanding of higher order processes is made possible, more DDCS_p at different energy losses would provide further guidance to theory in its efforts to advance our understanding of the collision dynamics. Energy losses corresponding to $v_e/v_p > 1$ would be of interest to test whether the average scattering angle of H follows the same trend as for H₂ [89] for $v_e/v_p > 1$.

For an ultimate test of the theoretical description of the few-body dynamics in atomic ionization FDCS measurements for p + H collisions are needed. Fully differential cross sections, $\frac{d\sigma^3}{d\Omega_p d\Omega_e dE_e}$, require the measurement of the electron solid angle along with the previously measured projectile solid angle and energy loss. This requires analyzing the recoil-ion momentum with significantly better resolution than accomplished at the time the experiment reported in this dissertation was performed. However, since then, the recoil-ion momentum resolution has been drastically improved and FDCS measurements are now being initiated. Figure 6.1 shows the improved resolution of the longitudinal recoil-ion momentum distribution, which is a critical step in attaining FDCS. With the previous resolution (a), there is a single, broad distribution, whereas, with the current resolution, there is a discrete peak due to electron capture along a well-separated spectrum due to ionization. From the width of the capture peak, one obtains an upper limit for the recoil-ion momentum resolution of about 0.15 a.u., which is good enough resolution to attain a FDCS for the p + H collision.

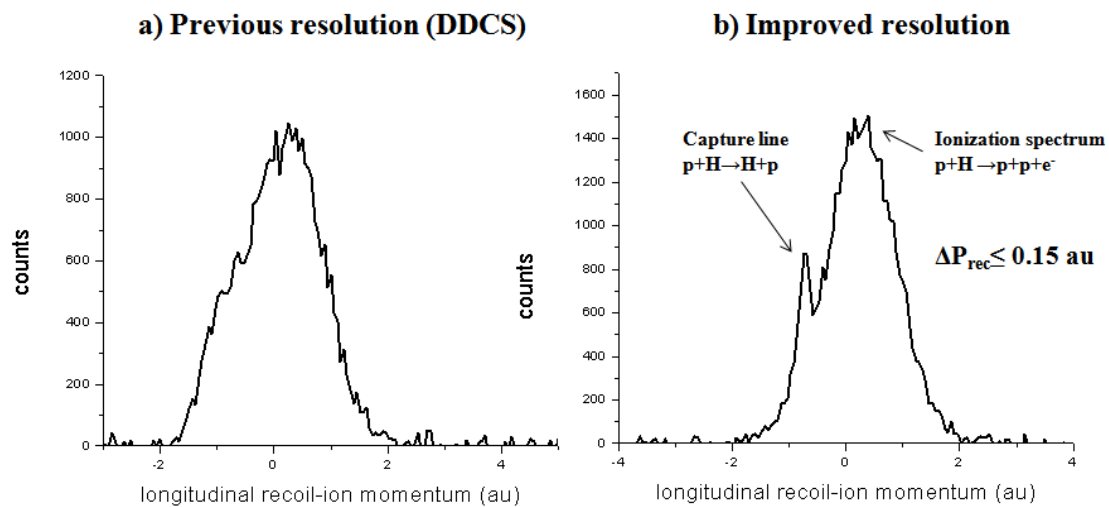


Figure 6.1. Longitudinal recoil-ion momentum distribution with the previous resolution (a)(used in this dissertation) and current resolution(b).

BIBLIOGRAPHY

- [1] E. Rutherford, *Philos. Mag.* **21**, 669 (1911)
- [2] M. Schulz, R. Moshhammer, D. Fischer, H. Kollmus, D.H. Madison, S. Jones, and J. Ullrich, *Nature* **422**, 48 (2003)
- [3] T.N. Rescigno, M. Baertschy, W.A. Isaacs, and C.W. McCurdy, *Science* **286**, 2474 (1999)
- [4] H. Ehrhardt, M. Schulz, T. Tekaath, and K. Willmann, *Phys. Rev. Lett.* **22**, 89 (1969)
- [5] H. Ehrhardt, K. Jung, G. Knoth, and P. Schlemmer, *Z. Phys.* **D1**, 3 (1986) (and references therein)
- [6] M. Schulz, R. Moshhammer, D.H. Madison, R.E. Olson, P. Marchant, C.T. Whelan, S. Jones, M. Foster, H. Kollmus, A. Cassimi, and J. Ullrich, *J. Phys.* **B34**, L305 (2001)
- [7] D. Fischer, R. Moshhammer, M. Schulz, A. Voitkiv, and J. Ullrich, *J. Phys.* **B36**, 3555 (2003)
- [8] M. Schulz, R. Moshhammer, D. Fischer, and J. Ullrich, *J. Phys.* **B36**, L311 (2003)
- [9] D. Fischer, M. Schulz, Moshhammer, and J. Ullrich, *J. Phys.* **B37**, 1103 (2004)
- [10] M. Schulz, R. Moshhammer, A. Voitkiv, B. Najjari, and J. Ullrich, *Nucl. Instrum. Meth.* **B235**, 296 (2005)
- [11] N. V. Maydanyuk, A. Hasan, M. Foster, B. Tooke, E. Nanni, D. H. Madison, and M. Schulz, *Phys. Rev. Lett.* **94**, 243201 (2005)
- [12] J. Ullrich, R. Moshhammer, R. Dörner, O. Jagutzki, V. Mergel, H. Schmidt-Böcking and L. Spielberger, *J. Phys. B: At. Mol. Opt. Phys.* **30** 2917 (1997)
- [13] R. Dörner, V. Mergel, O. Jagutzki, L. Spielberger, J. Ullrich, R. Moshhammer and H. Schmidt-Böcking, *Physics Reports* **330** 192 (2000)
- [14] I. Bray, *Phys. Rev. Lett.* **89**, 273201 (2002)
- [15] J. Colgan and M.S. Pindzola, *Phys. Rev.* **A74**, 012713 (2006)
- [16] M.S. Pindzola, F. Robicheaux, and J. Colgan, *J. Phys.* **B40**, 1695 (2007)

- [17] T.G. Lee, S. Yu. Ovchinnikov, J. Sternberg, V. Chupryna, D.R. Schultz, J.H. Macek, Phys. Rev. **A76**, 050701 (2007)
- [18] V.D. Rodríguez and R.O. Barrachina, Phys. Rev. **A57**, 215 (1998)
- [19] D.H. Madison, M. Schulz, S. Jones, M. Foster, R. Moshhammer, and J. Ullrich, J. Phys. **B35** 3297 (2002)
- [20] C.T. Whelan, R. J. Allan, H.R.J. Walters, and X. Zhang, in Whelan et al (Editors), *(e,2e) & related processes*, (Kluwer, Dordrecht), 1-32 (1993)
- [21] M. Schulz, R. Moshhammer, A.N. Perumal, and J. Ullrich, J. Phys. **B35**, L161 (2002)
- [22] A. Hasan, N.V. Maydanyuk, B.J. Fendler, A. Voitkiv, B. Najjari, and M. Schulz, J. Phys. **B37**, 1923 (2004)
- [23] M. Schulz, A. Hasan, N.V. Maydanyuk, M. Foster, B. Tooke, and D.H. Madison, Phys. Rev. **A73**, 062704 (2006)
- [24] M. Schulz and D.H. Madison, International Journal of Modern Physics **A21**, 3649 (2006) (and references therein)
- [25] M. Schulz, R. Moshhammer, D. Fischer, D.H. Madison, A. Hasan, N.V. Maydanyuk, and J. Ullrich, Recent Research Developments in Physics **5**, Transworld Research Network, Trivandrum, India, 679-701 (2004) (and references therein)
- [26] D. H. Madison, D. Fischer, M. Foster, M. Schulz, R. Moshhammer, S. Jones, and J. Ullrich, Phys. Rev. Lett. **91**, 253201 (2003)
- [27] M. Foster, J. L. Peacher, M. Schulz, D. H. Madison, Z. Chen, and H. R. J. Walters, Phys. Rev. Lett. **97**, 093202 (2006).
- [28] A.B. Voitkiv, B. Najjari, R. Moshhammer, M. Schulz, and J. Ullrich, J. Phys. **B37**, L365 (2004)
- [29] M. Dürr, C. Dimopoulou, B. Najjari A. Dorn, and J. Ullrich, Phys. Rev. Lett. **96**, 243202 (2006)
- [30] M. Dürr, C. Dimopoulou, A. Dorn, B. Najjari, I. Bray, D.V. Fursa, Z. Chen, D.H. Madison, K. Bartschat and J. Ullrich, J. Phys. **B39**, 4097 (2006)
- [31] M. Dürr, C. Dimopoulou, B. Najjari, A. Dorn, K. Bartschat, I. Bray, D.V. Fursa, Zh. Chen, D.H. Madison, and J. Ullrich, Phys. Rev. **A77**, 032717 (2008)
- [32] R.W. van Boeyen, N. Watanabe, J.W. Cooper, J. P. Doering, J. H. Moore, and M. A. Coplan, Phys. Rev. **A73**, 032703 (2006)

- [33] R.E. Olson and J. Fiol, Phys. Rev. Lett. **95**, 263203 (2005)
- [34] S. Otranto, R.E. Olson, and J. Fiol, J. Phys. **B39**, L175 (2006)
- [35] J. Fiol, S. Otranto, and R.E. Olson, J. Phys. **B39**, L285 (2006)
- [36] M. Dürr, B. Najjari, M. Schulz, A. Dorn, R. Moshhammer, A.B. Voitkiv, and J. Ullrich, Phys. Rev. **A75**, 062708 (2007)
- [37] M. Schulz, M. Dürr, B. Najjari, R. Moshhammer, J. Ullrich, Phys. Rev. **A76**, 032712 (2007)
- [38] W.L. Fite, R.T. Brackmann, and W.R. Snow, Phys. Rev. **112**, 1161 (1958)
- [39] G.W. McClure, Phys. Rev. **148**, 47 (1966)
- [40] J.E. Bayfield, Phys. Rev. **185**, 105 (1969)
- [41] J. T. Park, J. E. Aldag, J. M. George, and J. L. Peacher, Phys. Rev. **A14**, 608 (1976)
- [42] T.J. Morgan, J. Geddes, H.B. Gilbody, J. Phys. **B6**, 2118 (1973)
- [43] W.L. Fite, R.F. Stebbings, D.G. Hummer, and R.T. Brackmann, Phys. Rev. **119**, 663 (1960)
- [44] M.B. Shah and H.B. Gilbody, J. Phys. **B14**, 2361 (1981)
- [45] M.E. Rudd, Y.K. Kim, D.H. Madison, and J.W. Gallagher, Rev. Mod. Phys. **57**, 965 (1985) (and references therein)
- [46] G.W. Kerby, M.W. Gealy, Y.-Y. Hsu, M.E. Rudd, D.R. Schultz, and C.O. Reinhold, Phys. Rev. **A51** 2256 (1995)
- [47] Y.-Y. Hsu, M.W. Gealy, G.W. Kerby, M.E. Rudd, D.R. Schultz, and C.O. Reinhold, Phys. Rev. **A53** 303 (1996)
- [46] L.C. Tribedi, P. Richard, Y. D. Wang, C. D. Lin, and R. E. Olson, Phys. Rev. Lett. **77**, 3767 (1996)
- [47] H. Vogt, R. Schuch, E. Justiniano, M. Schulz, and W. Schwab Phys. Rev. Lett. **57**, 2256 (1986)
- [48] J.T. Park, J.E. Aldag, J.M. George, and J. L. Peacher, Phys. Rev. Lett. **34**, 1253 (1975)
- [49] J.T. Park, J.E. Aldag, J.M. George, and J. L. Peacher, Phys. Rev. **A15**, 608 (1977)

- [50] E. Edgu-Fry, A. Wech, J. Stuhlman, T.G. Lee, C.D. Lin, and C.L. Cocke, Phys. Rev. **A69**, 052714 (2004)
- [51] T. Vajnai, A.D. Gaus, J.A. Brand, W. Htwe, D.H. Madison, R.E. Olson, J.L. Peacher, and M. Schulz, Phys. Rev. Lett. **74**, 3588 (1995)
- [52] M. Schulz, T. Vajnai, A.D. Gaus, W. Htwe, D.H. Madison, and R.E. Olson, Phys. Rev. **A54** 2951 (1996)
- [53] J. Röder, H. Ehrhardt, I. Bray, D.V. Fursa, and I.E. McCarthy, J. Phys. **B29**, 2103 (1996)
- [54] J.G. Childers, K.E. James, M. Hughes, I. Bray, M. Baertschy, and M.A. Khakoo Phys. Rev. **A68**, 030702 (2003)
- [55] H. Knudsen and J.F. Reading, Phys. Rep. **212**, 107 (1992)
- [56] J.H. McGuire, N. Berrah, R.J. Bartlett, J.A.R. Samson, J.A. Tanis, C.L. Cocke, and A.S. Schlachter, J. Phys. **B28**, 913 (1995)
- [57] L. Rodberg and R. M. Thaler, *Introduction to the Quantum Theory of Scattering*, (Academic Press, New York, 1967) pp. 127-211
- [58] H. Bethe, Ann. Phys. Lpz. **5**, 325 (1930)
- [59] M. inokuti, Rev. Mod. Phys. **43**, 297 (1971) (and references therein)
- [60] W. Oldham, Phys. Rev. **140**, A1477 (1965)
- [61] W. Oldham, Phys. Rev. **161**, 1 (1967)
- [62] D.R. Bates and G. Griffing, Proc. Phys. Soc. **A66**, 961 (1953)
- [63] D.H. Madison, Phys. Rev. **A8**, 2449 (1973)
- [64] B. H. Bransden and C. J. Joachain, *Physics of Atoms and Molecules, 2nd Ed*, (Pearson Education, London, 2003) pp. 619-627
- [65] D.H. Madison and W.N. Shelton, Phys. Rev **A7**, 499 (1973)
- [66] I.M. Cheshire; Proc. R. Phys. Soc. **84**, 89 (1964)
- [67] Dz. Belkic; J. Phys. **B11**, 3529 (1978)
- [68] D.S.F. Crothers and J.F. McCann, J. Phys. **B16**, 3229 (1983)

- [69] P.D. Fainstein, V.H. Ponce, and R.D. Rivarola, *J. Phys.* **B24**, 3091 (1991) (and references therein)
- [70] Dz. Belkic, R. Gayet, and A. Salin, *Phys. Rep.* **56**, 279 (1979)
- [71] A.C. LaForge, K.N. Egodapitiya, J.S. Alexander, A. Hasan, M.F. Ciappina, M.A. Khakoo, and M. Schulz, *Phys. Rev. Lett.* **103**, 053201 (2009)
- [72] A.L. Godunov, Sh.D. Kunikeev, V.N. Mileev, and V.S. Senashenko, *Zh. Tekh. Fiz.* **53**, 436 (1983)
- [73] A.L. Godunov, Sh.D. Kunikeev, V.N. Mileev, and V.S. Senashenko, *Sov. Phys. JETP* **69**, 927 (1989)
- [74] M. Brauner, J.S. Briggs, and H. Klar, *J. Phys.* **B22**, 2265 (1989)
- [75] A.L. Godunov, V.A. Schipakov, and M. Schulz, *J. Phys.* **B31**, 4943 (1998)
- [76] J.T. Park and F.D. Schowengerdt, *Rev. Sci. Instrum.* **40**, 753 (1969)
- [77] A.D. Gaus, W. Htwe, J.A. Brand, T.J. Gay, and M. Schulz, *Rev. Sci. Instrum.* **65**, 3739 (1994)
- [78] K. Wien, *Braz. J. Phys.* **29**, 401 (1999)
- [79] B. Paolini and M.A. Khakoo, *Rev. Sci. Instrum.* **69**, 3121 (1998)
- [80] D.R. Miller, in *Atomic and Molecular Beam Methods*, edited by G. Scoles (Oxford University Press, New York, 1988), pp. 14-53
- [81] W.C. Wiley and I.H. McLaren, *Rev. Sci. Instrum.* **26**, 1150 (1955)
- [82] J.L. Wiza, *Nucl. Instrum. Meth.* **162**, 587 (1979)
- [83] O. Jagutzki, J.S. Lapington, L.B.C. Wirth, U. Spillman, V. Mergel, and H. Schmidt-Böcking, *Nucl. Instrum. Meth.* **A477**, 256 (2002)
- [84] J. Alexander, Ph.D. dissertation, Missouri University of Science & Technology (2009)
- [85] Atomic Data for Fusion, C.F. Barnett (ed.), Oak Ridge National Laboratory, **D6**, Oak Ridge (1990), <http://www-cfadc.phy.ornl.gov/redbooks/redbooks.html>
- [86] M.E. Rudd, Y.-K. Kim, D.H. Madison, and T.J. Gay, *Rev. Mod. Phys.* **64**, 441 (1992) (and references therein)

- [87] M. Schulz, A.C. Laforge, K.N. Egodapitiya, J.S. Alexander, A. Hasan, M.F. Ciappina, A.C. Roy, R. Dey, and A.L. Godunov, to be submitted to Phys. Rev. A
- [88] E.Y. Kamber, C.L. Cocke, S. Cheng, and S.L. Varghese, Phys. Rev. Lett. **60**, 2026 (1988)
- [89] J.S. Alexander, A.C. Laforge, A. Hasan, Z.S. Machavariani, M.F. Ciappina, R.D. Rivarola, D.H. Madison, and M. Schulz, Phys. Rev. **A78**, 060701(R) (2008)
- [90] R. Dey, A.C. Roy, and C. Dal Cappello, Nucl. Instrum. Meth. **B266**, 242 (2008)
- [91] Y.E. Kim and A.L. Zubarev, Phys. Rev. **A56**, 521 (1997)
- [92] S. Jones and D.H. Madison, Phys. Rev. **A62**, 042701 (2000)
- [93] R. Dey and A.C. Roy, Nucl. Instrum. Meth. **B243**, 28 (2006)

VITA

Aaron Christopher LaForge was born in Kansas City, Missouri on November 28, 1981. After graduating from Nixa High School in Nixa, Mo in 2000, Aaron went to Drury University in Springfield, Mo. In December 2004, he graduated Magna Cum Laude with a Bachelor of Arts in Physics with a minor in Global Studies. The following semester, Aaron enrolled at Missouri University of Science & Technology where he obtained a PhD in Physics in May 2010.

While at MS&T, Aaron published three peer-reviewed articles, one of which in Physical Review Letters. He has presented his research at eight national and international conferences including an invited talk at the 21st International Symposium of Ion-Atom Collisions in Norfolk, VA. Aaron also has an upcoming invited talk at the 63rd Annual Gaseous Electronics Conference in Paris, France.

Aaron was awarded the Chancellor's Fellowship, won the 2010 Scheerer's Prize, was a finalist for best student research at the 62nd Annual Gaseous Electronics Conference in Saratoga Springs, NY, and was invited to attend the 60th Meeting of Nobel Laureates in Lindau, Germany. From 2006 to 2008, he was the Physics department representative in the Council of Graduate Students at MS&T.

